

# Improved Stark Broadened Profiles for Neutral Helium Lines Using Computer Simulations

PATRICK TREMBLAY,<sup>1</sup> ALAIN BEAUCHAMP,<sup>1</sup> PIERRE BERGERON,<sup>1</sup> AND ANTOINE BÉDARD<sup>2</sup>

<sup>1</sup>*Département de Physique, Université de Montréal, C.P. 6128, Succ. Centre-Ville, Montréal, Québec H3C 3J7, Canada*

<sup>2</sup>*Department of Physics, University of Warwick, Coventry CV4 7AL, UK*

## ABSTRACT

The study of Stark broadening of neutral helium lines, despite significant advances over recent decades, has not led to updated large grids of helium line profiles relevant to the spectroscopic study of helium-rich stars. While the semi-analytical approach based on the standard Stark broadening theory is efficient for generating such grids, it presents challenges in incorporating additional physical effects into the model. Motivated by recent studies that highlight potential issues with line profiles in the context of white dwarf stars, this paper leverages advances in computer simulations to create a new grid of line profiles for 13 neutral helium lines in the optical range. These profiles cover densities ranging from  $10^{14}$  to  $6 \times 10^{17}$   $\text{cm}^{-3}$  and temperatures from 10,000 K to 40,000 K, with the exception of the narrower He I  $\lambda 4713$  line, for which the profile grid begins at  $10^{15.5}$   $\text{cm}^{-3}$ . The primary goal of this research is to present the new grid and compare it with both the semi-analytical approach and other simulation results. By doing so, corrections to the previous grid will be explored, providing a foundation for future studies that utilize this updated grid. We also examine the impact of these new profiles on the determination of physical parameters for a range of astrophysical objects, including DB white dwarfs and other helium-rich stars.

*Keywords:* White dwarf stars (1799) — Collisional broadening (2083) — Astrophysical processes (104) — Spectroscopy (1558) — N-body simulations (1083)

## 1. INTRODUCTION

Recent studies on white dwarf stars (Bergeron et al. 2011; Genest-Beaulieu & Bergeron 2019; Bergeron et al. 2019; Cukanovaite et al. 2021) have revealed challenges in determining physical parameters using traditional methods, specifically the photometric and spectroscopic techniques (see, e.g., Bergeron et al. 1997 and Bergeron et al. 1992, respectively). The photometric technique relies on fitting the overall spectral energy distribution, while the spectroscopic technique focuses on fitting individual line profiles, making it more sensitive to atomic physics details. In an effort to reconcile the physical parameters derived from both methods, several lines of investigation have been proposed, including a thorough review of the line profile grids used in spectroscopic analyses. For helium-line DB white dwarfs, these grids originate from the work of Beauchamp et al. (1997, hereafter B97). Although this grid has been dependable over the years, a timely update is essential to align with modern calculations. This effort began with the study by Trem-

blay et al. (2020), which utilized computer simulations. Our goal is to advance this initiative by providing a major update to the simulation-based line profiles, incorporating improvements suggested by Rosato et al. (2020) and Cho et al. (2022).

The computer simulation method for generating line profiles is not new; it has existed since the time when semi-analytical methods based on the standard Stark broadening theory were the preferred option (B97). However, it has consistently been constrained by its computational and time-intensive demands. The original motivations behind using simulations were twofold: to go beyond the impact approximation for electrons, and to model the effects of ion dynamics on line profiles, a factor often neglected in most studies relying on semi-analytical profiles (with the exception of Barnard et al. 1974 and Barnard et al. 1975, who generated exhaustive line profile grids for He I  $\lambda\lambda 4471$  and 4922).

The foundational work on the computer simulation method was introduced by Stamm & Voslamber (1979), Stamm & Smith (1984), and later refined by Hegerfeldt & Kesting (1988). It was not until the advancements introduced by Gigosos et al. (1985) and Gigosos & Car-

denoso (1987) that the simulation approach gained significant attention. Following these developments, many efforts were made to improve the balance between computational time and the quality of the line profiles generated through simulations (Calisti et al. 1988; Frerichs 1989; Alexiou et al. 1999a,b). This progress was particularly evident in studies focused on the hydrogen atom (Gigosos & Cardenoso 1996; Halenka & Olchawa 1996; Sorge & Günter 2000; Olchawa 2002; Wujec et al. 2002; Halenka et al. 2002; Gigosos et al. 2003; Olchawa et al. 2004; Ferri et al. 2014; Gomez 2017) and the helium atom (Gigosos & González 2009; Lara et al. 2012; Tremblay et al. 2020) as emitters.

All of these efforts used the autocorrelation function approach to generate line profiles. However, some lines showed significant noise in the final results (Tremblay et al. 2020), especially in the far wings, a finding later confirmed mathematically by Rosato et al. (2020) and demonstrated by Cho et al. (2022) for hydrogen lines. These key studies highlight the importance of directly applying the power spectrum equation for line profile generation, avoiding the use of the autocorrelation function. This shift enhances the time-quality ratio of the method.

We begin in Section 2 by outlining the theoretical framework of the standard Stark broadening theory, along with the simulation methodology and its implementation details, including the power spectrum method and the particle-generation procedure. Section 3 then concentrates on the extraction of He I line profiles and presents intermediate validation results. The subsequent analysis offers a detailed comparison between the simulated line profiles and previously published calculations. In Section 4, we examine the potential impact of these new profiles on the determination of physical parameters for a range of astrophysical objects, including DB white dwarfs and other helium-rich stars. Concluding remarks are finally presented in Section 5.

## 2. THEORETICAL BACKGROUND

### 2.1. Standard Stark Broadening Theory

Following the formulation introduced by Anderson (1949), the spectral line shape can be expressed as the real part of the Fourier transform of the autocorrelation function  $C(t)$ :

$$I(\omega) = \frac{1}{\pi} \text{Re} \int_0^{\infty} dt e^{i\omega t} C(t), \quad (1)$$

where the autocorrelation function is given by

$$C(t) = \sum_{ab} \rho_a \langle a | \mathbf{d} | b \rangle \cdot \left\{ \langle a | U^\dagger(t, 0) \mathbf{d} U(t, 0) | b \rangle \right\}_{av}. \quad (2)$$

Here, the states  $|a\rangle$  and  $|b\rangle$  correspond to the upper and lower levels of the radiative transition of interest,  $\rho_a$  denotes the statistical weight of state  $a$ , and  $\mathbf{d}$  is the dipole operator in the Schrödinger picture. The operator  $U(t, 0)$  represents the time evolution of the emitter under the influence of external perturbations and is governed by the total Hamiltonian

$$H = H_0 + V(t), \quad (3)$$

where  $H_0$  is the unperturbed atomic Hamiltonian and  $V(t)$  describes the time-dependent interaction with the surrounding plasma perturbers. The expression for  $C(t)$  includes a thermal average over all dynamical configurations of the perturbers, which generally comprise both electrons and ions.

In the standard Stark broadening theory, the large disparity between the characteristic velocities of electrons and ions is exploited by adopting the quasi-static approximation for the slowly moving ions and the impact approximation for the rapidly moving electrons (Baranger 1958a, 1962; Smith et al. 1969; Barnard et al. 1969; Sahal-Brechot 1969a,b; Griem 1974; Gigosos 2014).

By neglecting interactions between ions and electrons, the thermal average can be factorized into independent averages over ionic and electronic configurations. As a result, the average over static ion configurations can be reformulated as an average over ion-induced electric fields, weighted by the microfield distribution function  $W_R(F)$ . This distribution accounts for spatial correlations among ions arising from their mutual Coulomb interactions and is characterized by the parameter  $R$ , defined as the ratio of the mean interionic distance to the Debye radius (Hooper 1968).

Within this framework, the autocorrelation function governing the spectral line profile becomes

$$C(t) = \int_0^{\infty} dF W_R(F) C_e(t; F)_{av_e}, \quad (4)$$

where  $C_e(t; F)$  denotes the electron-induced autocorrelation function in the presence of a static electric field  $F$ . The function  $C_e(t; F)$  retains the same formal structure as Equation (2), with the thermal average now restricted to the ensemble of electron trajectories. The corresponding time evolution is governed by the Hamiltonian

$$H(t) = H_0 + eFZ + V_e(t), \quad (5)$$

which includes a constant electric field  $F$  aligned along the  $z$ -axis,  $Z$  the  $z$ -component of the position operator of the emitting electron, and the time-dependent interaction  $V_e(t)$  between the emitter and the electrons.

The evolution operator associated with Equation (5) is evaluated within the framework of the impact approximation. This approximation relies on three key assumptions: (1) strong collisions are temporally isolated and do not overlap, (2) the cumulative effect of weak, overlapping collisions can be adequately described by truncating the Dyson series at second order, and (3) the characteristic collision duration is much shorter than the inverse of the spectral line half width at half maximum (the completed collision assumption).

After performing the thermal average over electron trajectories and applying the inverse Fourier transform defined in Equation (1), the resulting spectral line profile is obtained as

$$I(\omega) = \int_0^\infty dF W_R(F) I_e(\omega; F), \quad (6)$$

which represents a weighted superposition of electron-broadened line profiles corresponding to fixed values of the ionic microfield  $F$ .

Each component profile  $I_e(\omega; F)$  is given by

$$I_e(\omega; F) = -\frac{1}{\pi} \sum_{\alpha\alpha'\beta\beta'} \langle\alpha|\mathbf{d}|\beta\rangle\langle\beta'|\mathbf{d}|\alpha'\rangle \langle\alpha|\langle\beta| [i(\omega - \omega_{\alpha\beta}) + \Phi]^{-1} |\alpha'\rangle|\beta'\rangle, \quad (7)$$

where  $\omega_{\alpha\beta}$  denotes the transition frequency between the perturbed upper and lower states  $|\alpha\rangle$  and  $|\beta\rangle$ , respectively. The operator  $\Phi$  encapsulates the electron-induced broadening effects within the impact approximation. For clarity, the dependence of the perturbed states, energy levels, and the operator  $\Phi$  on the electric field  $F$  is not explicitly indicated. It is further assumed in this work that all upper states share the same statistical weight, which can therefore be omitted, as it cancels out when the final profile is normalized to unity.

Within the impact approximation, the collision operator  $\Phi$  is obtained by integrating over the full trajectory of a single electron and subsequently averaging over all possible trajectories. Under the classical path approximation, the electron is assumed to follow a straight-line trajectory at constant velocity. The averaging procedure therefore involves integration over all such trajectories, parameterized by three angular variables, the electron velocity  $v$ , the impact parameter  $\rho$ , and the time of closest approach. The integral over  $\rho$  exhibits formal divergences at both small and large values, which are treated by introducing appropriate cut-offs to ensure convergence in practical calculations.

In the far wings of the spectral line, the assumptions underlying the completed collision approximation of impact theory break down. In this regime, the one-electron theory developed by Baranger (1962) provides a more

appropriate description. This approach accounts for the contribution of isolated, non-overlapping strong collisions and describes the gradual transition of the line shape toward a quasi-static profile. Within the one-perturber framework, the definition of the collision operator  $\Phi$  differs from that employed in the standard impact theory. Notably, no rigorous theoretical prescription exists for smoothly connecting the two regimes. A practical implementation of this hybrid approach is described in B97.

Over the past three decades, spectroscopic analyses of DB white dwarfs have relied on the He I line profile tables of B97. These tables have also been employed in more recent studies of other classes of stars (Przybilla et al. 2021; Jeffery et al. 2024; Latour et al. 2025). The profiles were computed using the standard Stark broadening theory as implemented by Barnard et al. (1969) and Barnard & Cooper (1970), with the inclusion of the one-electron theory of Baranger (1962). Line dissolution was incorporated following the prescription of Seaton (1990), by restricting the integral in Equation (6) to electric field strengths below the critical value above which the upper levels of the transition are dissolved.

The limitations of the standard theory outlined above underscore the need to update existing grids of line profiles. In the context of DB white dwarfs, the far wings of the line profiles contribute to the pseudo-continuum and can influence the atmospheric parameters derived using the spectroscopic method. The treatment of the transition between the impact and one-electron regimes therefore introduces a source of uncertainty in this region. Moreover, for the spectral analysis of lower-density objects, such as main-sequence and helium-rich stars, ion dynamics can significantly affect the line core and, when present, the forbidden components. More generally, conclusions drawn from analyses based on the B97 profile tables should be reassessed using more modern calculations.

The objective of the simulation method presented in this work is to eliminate most of the approximations inherent in the standard Stark broadening theory while preserving the essential features of the semi-classical framework (see below). As such, this method is well suited to generate a new generation of Stark-broadened He I line profiles.

## 2.2. Computer Simulations

Computer simulations currently represent the state of the art for the calculation of Stark-broadened line profiles. This approach has been successfully applied to numerous hydrogen lines (Gigosos & Cardenoso 1996; Cho et al. 2022) as well as to neutral helium lines (Gigosos

& González 2009; Lara et al. 2012; Gigosos et al. 2014; Tremblay et al. 2020). Compared to the standard Stark broadening theory, computer simulations mitigate several inherent approximations, at the expense of a substantially increased computational cost. Nevertheless, the method remains sufficiently efficient to allow the generation of extensive grids of line profiles covering the wide range of thermodynamic conditions encountered in stellar atmospheres.

Unlike the standard theory, the simulation method correctly handles the superposition of collisions regardless of their duration and is not restricted to a perturbative treatment. In particular, the transition between the two electron-broadening regimes—namely, the impact regime dominating the line core and the one-electron regime relevant in the wings—as well as ion dynamics, are treated naturally within a unified framework that explicitly follows the time evolution of all perturbers. At the same time, computer simulations retain several advantages of the standard theory, most notably the ability to model forbidden components, which play a crucial role in the formation of helium line profiles. Indeed, many forbidden components are observed in the spectra of DB white dwarfs (Liebert et al. 1976; Beauchamp et al. 1995) and other helium-rich stars (Jeffery 1998; Przybilla et al. 2021).

The simulation method relies on the validity of the semi-classical approximation, in which the emitting atom is treated as a quantum subsystem immersed in a time-varying electric field generated by well-localized charged perturbers. These perturbers follow classical trajectories determined by their respective charges and by the charge state of the emitter. When the emitter is neutral, the perturbers move along straight-line trajectories at constant velocity.

The line profile associated with a given radiative transition is obtained as an arithmetic average over a large ensemble of dynamic perturber configurations. Each configuration produces a temporal sequence of electric fields that perturb the emitting atom. For a given temporal sequence, the Hamiltonian governing the evolution of the emitter is still given by Equation (3). In the present work, only the first nonvanishing term of the multipole expansion of the interaction  $V(t)$  is retained, namely the dipole term:

$$V(t) = e\mathbf{F}(t) \cdot \mathbf{R} \quad (8)$$

where  $\mathbf{F}(t)$  denotes the electric field at the position of the emitter and  $\mathbf{R}$  is the position operator of the radiating electron. Higher-order terms in the multipole expansion have been considered by some authors in the case of hydrogen lines (Cho et al. 2022).

The analysis of the electric field fluctuations experienced by the emitter is restricted to contributions from charged particles located within a spherical region, referred to as the simulation volume, whose radius is of the order of the Debye length. The generation of a temporal sequence of electric fields involves two distinct steps: the initialization of a distribution of charged perturbers and the reinjection of new perturbers as the simulation proceeds. During initialization, perturbers of the relevant species are placed within the simulation volume with initial position and velocity vectors drawn from a random number generator in a manner consistent with Boltzmann statistics. As time evolves, particles initially present within the simulation volume may exit the sphere and are replaced by new particles of the same type. This reinjection procedure ensures that the joint statistical distribution of particle positions and velocities remains stationary over time. Throughout the simulation, the emitting atom is fixed at the center of the sphere.

The assumption of negligible interactions among perturbers implies straight-line trajectories within the simulation volume, which does not fully reflect the physical conditions of a plasma. To account for inter-particle interactions at least at a first-order level, a Debye-screened Coulomb potential is employed to describe the electrostatic interaction between the perturbers and the emitter (Gigosos et al. 2003; Stambulchik et al. 2007), with the Debye length computed under the assumption of electron and ion screening. The statistical distribution of the magnitude of the electric fields generated at the center of the simulation volume, obtained from the ensemble of perturber configurations, is found to be consistent with the expected microfield distribution for a neutral emitter under the corresponding thermodynamic plasma conditions (Gigosos & Cardeñoso 1996; Cho et al. 2022). Moreover, this potential ensures that the electric field produced by an individual perturber in the immediate vicinity of the emitter remains Coulombian, as physically required.

Within the simulation framework, the thermal average over all perturbers appearing in Equation (2) is approximated by an average over a large but finite number  $N$  of dynamic configurations. The autocorrelation function  $C(t)$  is therefore computed as the mean of  $N$  individual autocorrelation functions  $C_i(t)$ , each corresponding to a specific configuration  $i$ . As time increases, the dipole moment of the emitter becomes progressively decorrelated from its initial value, causing the contribution of the integral to diminish and eventually approach zero; at this point,  $C(t)$  can be considered converged. An analysis of the convergence behavior of  $C(t)$  thus provides

a practical criterion for defining the upper integration limit in Equation (1), corresponding to the total duration of the simulation.

Alternatively, the line profile can be computed using the power spectrum method. As shown by Rosato et al. (2020) and Cho et al. (2022), this approach yields a significantly improved signal-to-noise ratio compared to the direct autocorrelation method. For this reason, the power spectrum method is adopted in the present work to compute the line profiles. Nevertheless, the autocorrelation function remains useful for determining the total simulation duration for a given simulation volume, that is, the number of time steps required for a chosen time step  $\Delta_t$ .

### 2.3. The Power Spectrum Method

Using the same notation as in Equation (2), the power spectrum associated with a given line transition is defined as

$$P(\omega) \propto \omega^4 \lim_{T \rightarrow +\infty} \frac{1}{T} \sum_{ab} \rho_a \left\langle \left| \int_{-T/2}^{T/2} dt \langle b | \mathbf{d}(t) | a \rangle e^{i\omega t} \right|^2 \right\rangle_{\text{av}}, \quad (9)$$

where  $\mathbf{d}(t)$  is the dipole operator of the emitting atom in the Heisenberg picture (Baranger 1958b, 1962; Rosato et al. 2020), and  $T$  denotes the time window over which the signal is observed or computed. The slowly varying prefactor  $\omega^4$  is omitted in the detailed calculations, yielding the line profile

$$I(\omega) \propto \lim_{T \rightarrow +\infty} \frac{1}{T} \sum_{ab} \rho_a \left\langle \left| \int_{-T/2}^{T/2} dt \langle b | \mathbf{d}(t) | a \rangle e^{i\omega t} \right|^2 \right\rangle_{\text{av}}, \quad (10)$$

which is subsequently normalized to unit area. Following the reasoning previously discussed for the autocorrelation function, the line profile is computed as the average of  $N$  individual realizations,

$$I(\omega) = \frac{1}{N} \sum_{i=1}^N I_i(\omega), \quad (11)$$

where  $I_i(\omega)$  is obtained from the  $i^{\text{th}}$  temporal sequence of dipole moments.

The power spectrum method is formally defined through the limiting process  $T \rightarrow +\infty$  (Equation 10). In practice, however, this formulation does not provide guidance on the minimum simulation duration required to obtain a profile free from numerical artifacts or systematic biases arising from the finite time window. An exploratory phase is therefore required to determine an appropriate value of  $T$  for each spectral line and set of thermodynamic conditions considered in this work.

Numerical tests performed on the He I  $\lambda 4471$  line show that the normalized profile intensity depends sensitively on the adopted value of  $T$ , particularly in the line wings at low electron density. For insufficient simulation durations, the wings are systematically overestimated, while the profile progressively converges toward its asymptotic shape as  $T$  increases. The formal limiting process is therefore unnecessary, provided that the simulation duration is chosen to be sufficiently long. This requirement must be assessed separately for each spectral line and set of plasma conditions (see Section 2.6 for details).

Because the reference time of the evolution operator is arbitrary in the Heisenberg representation, the final expression for the line profile corresponding to the  $i^{\text{th}}$  configuration becomes

$$I_i(\omega) \propto \sum_{ab} \rho_a \left| \int_0^T d\tau \langle b | \mathbf{d}(t) | a \rangle e^{i\omega\tau} \right|^2, \quad (12)$$

which remains fully compatible with the numerical simulation framework.

### 2.4. Generation and Reinjection of Particles

As described in previous studies (Gigosos & Cardenoso 1996; Tremblay et al. 2020; Cho et al. 2022), the simulation approach combines an initialization phase with a particle reinjection process. Perturbing particles—either charged ions or electrons—are initially placed inside a spherical simulation volume of radius  $R$  at  $t = 0$ . As the simulation evolves, particles that leave the volume are removed and replaced by new particles of the same species that enter the volume, while the emitting atom remains fixed at the center of the simulation sphere. Assuming a neutral emitter, the perturbers follow straight-line trajectories within the sphere,

$$\mathbf{r}(t) = b(\hat{v}_1 \cos \alpha + \hat{v}_2 \sin \alpha) + \hat{v}_3 v(t - t_0), \quad (13)$$

where  $v$  is the constant particle velocity,  $\hat{v}_3$  is the unit vector along the velocity direction,  $t_0$  is the time of closest approach,  $(\hat{v}_1, \hat{v}_2, \hat{v}_3)$  form an orthonormal basis, and the angle  $\alpha$  specifies the orientation of the trajectory in the plane defined by the velocity vector and the point of closest approach of magnitude  $b$ . Once a particle exits the simulation volume, it is removed from the simulation and does not re-enter.

The particle generation procedure is designed to ensure that, within a given simulation volume, the statistical properties of the system are preserved at all times and across all simulations running in parallel. In particular, the random generation of the angle  $\alpha$  and of the orthonormal basis ensures isotropy and homogeneity during both the initialization phase and the reinjection process.

At initialization, the joint probability distribution of  $t_0$ ,  $b$ , and  $v$  is given by

$$p(t_0, b, v) \propto bv^3 e^{-v^2/v_T^2}, \quad (14)$$

which can be expressed as the product of conditional distributions,

$$p(t_0, b, v) = p(t_0|b, v)p(b|v)p(v), \quad (15)$$

subject to the additional constraint that the perturbers must lie within the simulation volume,

$$|t_0| \leq t_{\max} \equiv \frac{\sqrt{R^2 - b^2}}{v}. \quad (16)$$

The joint distribution and the above constraint imply that

$$p(t_0|b, v) = \frac{1}{2t_{\max}} = \frac{v}{2\sqrt{R^2 - b^2}}, \quad (17)$$

which corresponds to a uniform distribution over the allowed range of  $t_0$ , and that

$$p(b|v) = \frac{3}{R^3} b \sqrt{R^2 - b^2} \equiv p(b), \quad (18)$$

which is independent of  $v$ , while  $v$  itself follows the Maxwell velocity distribution. Consequently, the variables  $v$  and  $b$  can be generated independently for each particle using random number generators. Once  $v$  and  $b$  are drawn, the corresponding value of  $t_{\max}$  is computed and  $t_0$  is sampled from a uniform distribution over the interval defined by Equation (16).

Since our previous work (Tremblay et al. 2020), several modifications have been introduced to the particle reinjection procedure to improve its physical realism. The method described by Tremblay et al. was based on the approach originally proposed by Gigosos & Cardeñoso (1996). Its main conceptual limitation is that it enforces fluctuation-free distributions during the simulation: the Maxwell velocity distribution and the corresponding distribution of the distance of closest approach  $b$  are satisfied exactly at all times.

A more physically faithful approach, recently demonstrated by Cho et al. (2022), is adopted here. The key idea is that the statistical distributions of the velocity  $v$  and impact parameter  $b$  for incoming particles must match those of the particles that leave the simulation volume. Particles with longer sphere-crossing times ( $2t_{\max}$ ) exit the volume less frequently. Consequently, the joint distribution  $p_{\text{in}}(v, b)$  of incoming particles must be proportional to the distribution of particles within the simulation volume at initialization, divided by the crossing time. This reasoning leads to

$$p_{\text{in}}(b|v) = \frac{2}{R^2} b \equiv p_{\text{in}}(b), \quad (19)$$

and

$$p_{\text{in}}(v) = \frac{2}{v_T^4} v^3 e^{-v^2/v_T^2}, \quad (20)$$

after proper normalization.

With this reinjection scheme, the sampled distributions of  $v$  and  $b$  at any given time are allowed to deviate slightly from their theoretical forms due to statistical fluctuations. This behavior is physically more realistic, as the distributions are respected on average rather than enforced deterministically. In addition, this approach naturally facilitates extensions to more general particle trajectories in future developments.

A further refinement of the reinjection process consists in allowing particles to be reinjected within a thin spherical shell, rather than strictly at the boundary of the simulation volume. The reinjected particle is placed within a shell of variable thickness determined by its velocity. The parameter  $t_0$  associated with a reinjected particle is then given by

$$t_0 = \frac{\sqrt{(R - \Delta r)^2 - b^2}}{v}, \quad (21)$$

where  $\Delta r$  is a uniformly distributed random variable in the interval  $[0, v\Delta_t]$ , representing the maximum distance the particle could have traveled during the time step  $\Delta_t$ . This correction prevents the reinjection of a new particle from coinciding exactly with the exit of another, while preserving a constant total number of particles at each discrete simulation time  $t_k$ .

## 2.5. Time Evolution Operator

In this work, all calculations are performed within the no-quenching approximation (Kolb & Griem 1958), which assumes that collisions do not induce transitions between states with different principal quantum numbers  $n$ . As a consequence, the matrix element of the dipole operator can be expanded over two disjoint sets of upper and lower states,  $|a'\rangle$  and  $|b'\rangle$ , which include all states sharing the same principal quantum number (and spin) as the states  $|a\rangle$  and  $|b\rangle$  involved in the radiative transition under consideration:

$$\langle b|\mathbf{d}(t)|a\rangle = \sum_{a'b'} \langle b|U_b^\dagger(t, 0)|b'\rangle \langle b'|\mathbf{d}|a'\rangle \langle a'|U_a(t, 0)|a\rangle. \quad (22)$$

Here,  $\mathbf{d}$  denotes the dipole moment operator in the Schrödinger picture, while  $U_a$  and  $U_b$  are the time evolution operators projected onto the upper and lower subspaces of states, respectively.

The projected evolution operators satisfy the equations

$$\begin{aligned} i\hbar \frac{dU_a(t, 0)}{dt} &= H_a(t) U_a(t) \\ i\hbar \frac{dU_b(t, 0)}{dt} &= H_b(t) U_b(t) \end{aligned} \quad (23)$$

where  $H_a$  and  $H_b$  are the projections of the total Hamiltonian (Equation 3) onto the corresponding subspaces. This formalism explicitly incorporates lower-state mixing in the simulations. While this effect was already included in earlier studies (Gigosos & Cardenoso 1996; Gigosos et al. 2014; Cho et al. 2022), it was neglected in the calculations of Tremblay et al. (2020).

Once a temporal sequence of electric fields has been generated at  $N_t$  consecutive time steps  $t_k \equiv k\Delta_t$  (with  $k$  ranging from 0 to  $N_t - 1$ ), the time evolution operators  $U_a(t_k, 0)$  and  $U_b(t_k, 0)$  of the perturbed atom must be evaluated in the corresponding upper and lower subspaces. Following Gigosos & Cardenoso (1996), we assume that the electric field—and therefore the Hamiltonian operator  $H$ —remains constant within each time interval  $(t_{k-1}, t_k)$ . Under this approximation, the operators  $U_a$  and  $U_b$  are diagonal in the basis of their respective instantaneous eigenstates:

$$\begin{aligned} \langle \alpha' | U_a(t_k, t_{k-1}) | \alpha \rangle &= e^{-iE_\alpha \Delta_t / \hbar} \delta_{\alpha\alpha'} \\ \langle \beta' | U_b(t_k, t_{k-1}) | \beta \rangle &= e^{-iE_\beta \Delta_t / \hbar} \delta_{\beta\beta'}. \end{aligned} \quad (24)$$

Here,  $E_\alpha$  and  $E_\beta$  denote the energies of the perturbed upper and lower states  $|\alpha\rangle$  and  $|\beta\rangle$ , respectively. This property allows the matrix elements of the operators  $U_a(t_k, t_{k-1})$  and  $U_b(t_k, t_{k-1})$  to be expressed in the basis of unperturbed states. For the upper states, one obtains

$$\langle \alpha' | U_a(t_k, t_{k-1}) | \alpha \rangle = \sum_{\alpha} e^{-iE_\alpha \Delta_t / \hbar} \langle \alpha' | \alpha \rangle \langle \alpha | \alpha \rangle, \quad (25)$$

where the perturbed-state energies  $E_\alpha$  and the transformation coefficients  $\langle \alpha | \alpha \rangle$  are obtained by solving the corresponding eigenvalue problem; an analogous expression applies to the lower states.

The full evolution operators  $U_a(t_k, 0)$  and  $U_b(t_k, 0)$  are then constructed iteratively by matrix multiplication:

$$\begin{aligned} \langle \alpha' | U_a(t_k, 0) | \alpha \rangle &= \\ & \sum_{\alpha''} \langle \alpha' | U_a(t_k, t_{k-1}) | \alpha'' \rangle \langle \alpha'' | U_a(t_{k-1}, 0) | \alpha \rangle \\ \langle \beta' | U_b(t_k, 0) | \beta \rangle &= \\ & \sum_{\beta''} \langle \beta' | U_b(t_k, t_{k-1}) | \beta'' \rangle \langle \beta'' | U_b(t_{k-1}, 0) | \beta \rangle. \end{aligned} \quad (26)$$

This numerical integration scheme preserves the unitarity of the time evolution operator by construction.

The validity of this procedure relies on the assumption that the electric field varies negligibly over a single time step  $\Delta_t$ . The time step is therefore chosen as a fraction  $\epsilon$  of the characteristic timescale associated with the temporal variation of the electric field,

$$\Delta_t = \epsilon \frac{r_0}{v_T}, \quad (27)$$

where  $r_0$  denotes the typical interparticle distance in a plasma of electron density  $N_e$ , and  $v_T$  is the electron thermal velocity, computed using the reduced mass  $\mu_e$ . Typical values of  $\epsilon$  used in previous studies are  $\epsilon = 0.01$  (Gigosos & Cardenoso 1996; Tremblay et al. 2020) and  $\epsilon = 0.05$  (Cho et al. 2022).

## 2.6. Implementation Details

The simulation method is computationally demanding, which makes the careful selection of its parameters essential. Choosing these parameters requires a delicate balance between achieving accurate line profiles and maintaining reasonable computational time. The main parameters of the model include the time step, controlled by the parameter  $\epsilon$  (see Equation 27), the total number of time steps  $N_t$ , the radius of the simulation volume  $R$ , expressed as a multiple  $K_D$  of the Debye radius,

$$R = K_D \sqrt{\frac{kT}{4\pi(N_e + N_{\text{HeII}})e^2}}, \quad (28)$$

and the number of independent time sequences of electric fields used to compute the final profile.

In previous work (Tremblay et al. 2020), the simulation volume and the calculation volume were treated as separate entities. The simulation volume contained all moving perturbers, while only those particles located within a smaller calculation volume contributed to the electric field at the position of the emitting atom. However, this approach introduces a significant computational overhead, especially at low electron densities. In the present study, we simplify the procedure by equating the simulation and calculation volumes. This modification eliminates unnecessary computations without compromising accuracy.

The choice of the multiple  $K_D$  is guided by two considerations: (1) the microfield distribution obtained from the simulation should closely match the theoretical microfield distribution of Hooper (1968), and (2) the temporal evolution of the electric field at the emitter must remain continuous when a perturber leaves the simulation volume and is replaced. Through extensive testing, we determined that  $K_D = 3$  provides satisfactory results

for electron densities below  $10^{17} \text{ cm}^{-3}$ , while  $K_D = 5$  is more appropriate for higher densities. Using a single value for all densities is problematic because, paradoxically, the number of perturbers within a sphere of fixed radius (in units of the Debye length) increases as the density decreases, leading to unnecessarily long computational times at low densities. Choosing an appropriate  $K_D$  ensures both physical accuracy and computational efficiency across the full range of densities considered.

Another key parameter is the exclusion radius, which defines the minimum allowed impact parameter in order to prevent unphysically large electric fields at the emitter. While one could, in principle, define the exclusion radius individually for each transition as the orbital radius of its upper energy levels, we adopt a uniform exclusion radius for all simulations. Specifically, we choose a value corresponding to the orbital size of the  $n = 2$  level of the helium atom. This choice provides a reasonable balance between accuracy and computational cost, while preventing extreme field contributions that could destabilize the simulation.

The time step  $\Delta_t$  and the total number of steps  $N_t$  must also be carefully selected. The initial goal is to determine values that are suitable for all spectral lines and thermodynamic conditions under consideration. Analysis of the autocorrelation function of the dipole moment,  $C(t)$ , indicates that the product  $N_t \epsilon$  must be chosen based on the narrowest spectral lines and the lowest electron densities in the grid. Based on tabulated Lorentzian widths computed using the standard theory (for example, Griem 1974), the He I  $\lambda 4713$  line is significantly narrower than other lines studied. Therefore, we divide the lines into two categories: He I  $\lambda 4713$  and broader lines.

For the broader lines, the value  $N_t \epsilon = 2000$  was adopted, determined from the autocorrelation function of the He I  $\lambda 4471$  line at the minimum electron density of  $10^{14} \text{ cm}^{-3}$ . This value ensures that the autocorrelation function has essentially decayed to zero at the end of the simulation duration,  $T = N_t \Delta_t(\epsilon)$ , guaranteeing convergence of the line profiles when computed using the power spectrum method.

The separate choice of  $N_t$  and  $\epsilon$  is then made with computational efficiency in mind. Following the approach of Tremblay et al. (2020), setting  $\epsilon = 0.01$  would lead to  $N_t = 200,000$ , which is computationally expensive. We therefore adopt  $\epsilon = 0.02$ , which reduces  $N_t$  to 100,000 while still maintaining adequate temporal resolution of the electric field variations. This choice represents a reasonable compromise between computational efficiency and the accuracy required to resolve the narrowest features of the spectral lines.

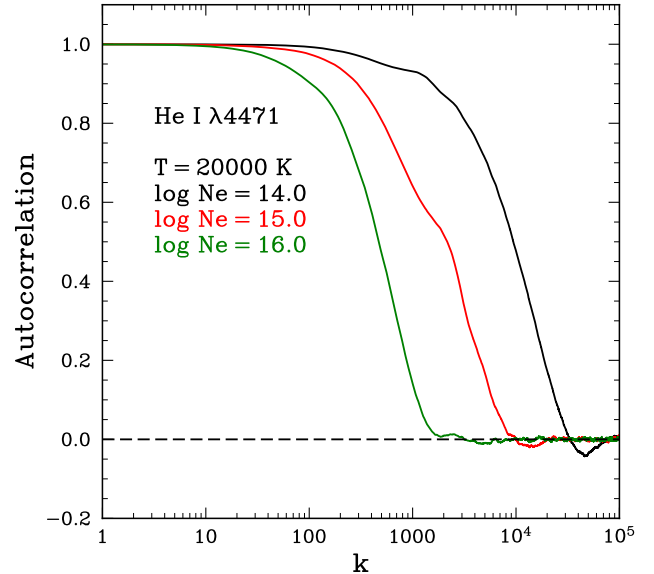


**Figure 1.** Autocorrelation function of He I  $\lambda 4471$  for  $T = 20,000 \text{ K}$  and electron densities  $10^{14}$ ,  $10^{15}$ , and  $10^{16} \text{ cm}^{-3}$  over the simulation time-step index  $k = t_k/\Delta_t$ .

Figure 1 illustrates the autocorrelation function of the He I  $\lambda 4471$  line at  $T = 20,000 \text{ K}$  for three different electron densities, plotted as a function of the logarithm of the time-step index  $k$  (defined as  $t_k \equiv k\Delta_t$  with  $k$  ranging from 0 to  $N_t - 1$ ). As implied by Equation 1, computing the line profile by integrating the autocorrelation function up to the finite duration of the simulation  $T$  is only valid if the autocorrelation function has effectively converged to zero over the integration domain. The characteristic width of the autocorrelation function increases as the electron density decreases, reflecting the slower decay of correlations at lower densities. This behavior imposes a lower limit on the density for which a given number of time steps is sufficient.

For the narrowest line, He I  $\lambda 4713$ , simulations at  $N_e = 10^{14} \text{ cm}^{-3}$  would require prohibitive simulation durations. Consequently, we only compute its profiles for  $N_e \geq 10^{15.5} \text{ cm}^{-3}$ , using the same  $N_t$  and  $\epsilon$  values as for broader lines. Figure 2 shows the autocorrelation function for this line at two electron densities. Three additional narrow lines, He I  $\lambda\lambda 3889$ , 5016, and 5876 were initially considered, but were excluded due to computational constraints.

The computation of the line profile  $I_i(\omega)$  for a given simulation volume proceeds in three main steps. First, the time sequence of electric fields,  $\mathbf{F}_i(t_k)$ , at the center of the simulation volume is generated from the spatial and temporal distribution of perturbers. Second, the Schrödinger equation (Equation 23) is integrated numerically within the upper and lower state subspaces, and

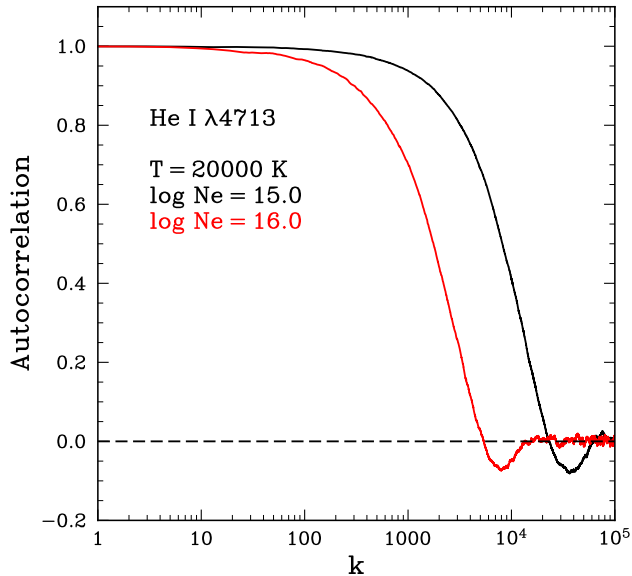


**Figure 2.** Same as Figure 1 but for He I  $\lambda 4713$  for  $T = 20,000$  K and electron densities  $10^{15}$  and  $10^{16}$   $\text{cm}^{-3}$ .

the evolution operator matrix elements are computed as in Equation 25. Finally, the time-dependent dipole matrix elements (Equation 22) are substituted into Equation 12, and the integral over time is performed for each required frequency to obtain the final line profile.

This implementation strategy ensures that all relevant physical effects—including ion dynamics, electron-impact broadening, and state mixing—are correctly captured while maintaining convergence and numerical stability across the full range of densities and line widths considered.

In summary, our improved profiles differ from those of Tremblay et al. (2020) in terms of the use of the power spectrum method, the particle reinjection procedure, the lower-state mixing, and the identity between the simulation and calculation volumes.

### 3. RESULTS

With the simulation environment and computational procedure now fully established, we turn to an analysis of the resulting line profiles.

All He I spectral lines considered in this work arise from transitions between upper levels  $|n\ell_a m_a s\rangle$  with  $3 \leq n \leq 6$  and lower levels  $|2\ell_b m_b s\rangle$  of identical spin  $s$ , for given values of  $\ell_a$  and  $\ell_b$ , within the wavelength range 3800–5100 Å. The transitions examined include  $2P^1 - nS^1$  ( $\lambda\lambda 5048, 4438, \text{ and } 4169$ ),  $2S^1 - nP^1$  ( $\lambda 3965$ ),  $2P^1 - nD^1$  ( $\lambda\lambda 4922, 4388, \text{ and } 4144$ ),  $2P^3 - nS^3$  ( $\lambda\lambda 4713, 4121, \text{ and } 3868$ ), and  $2P^3 - nD^3$  ( $\lambda\lambda 4471, 4026, \text{ and } 3820$ ). Most transitions of the form  $2S - nP$  lie in

the near-ultraviolet and were therefore excluded from the present analysis.

The spectral line profiles are computed at three temperatures: 10,000 K, 20,000 K, and 40,000 K. As discussed in Section 2.6, the narrowest transition, He I  $\lambda 4713$ , constitutes a particular case. For this line, profiles are calculated over an electron-density range of  $\log N_e = 15.5$  to 17.5 in steps of 0.5, with an additional calculation performed at  $6 \times 10^{17}$   $\text{cm}^{-3}$ , which matches the highest density tabulated by Shamey (1969) and Beauchamp et al. (1997). All remaining lines are also computed at lower densities, specifically  $\log N_e = 14.0, 14.5, \text{ and } 15.0$ . The perturber population consists of electrons and He II ions in equal proportions. Contributions from He III ions are neglected, as their number density is expected to be negligible under the thermodynamic conditions characteristic of DB white dwarf atmospheres and other stars studied in this work.

The comparison between the present set of line profiles and those available in the literature is carried out in two stages. We first concentrate on the two transitions for which profiles including ion dynamics are available, namely He I  $\lambda\lambda 4471$  and 4922. A more extensive comparison is then performed for all 13 lines using a new generation of profiles computed following the methodology of B97, which is based on the standard Stark broadening theory. For consistency, the reference profiles have been modified to establish a common baseline with the present calculations. In particular, the revised profiles exclude the effects of line dissolution and adopt a finer wavelength resolution, matching that employed in the numerical simulations. Although line dissolution is a well-established physical effect (Seaton 1990; Tremblay & Bergeron 2009; Gomez et al. 2017; Cho et al. 2022), it is not included in the current simulation framework.

Under these conditions, any remaining discrepancies between the simulated profiles and those derived from standard theory are expected to originate primarily from the explicit treatment of ion dynamics, and possibly from differences in the modeling of electron broadening in the line wings. In the work of B97, an interpolation between the one-electron approximation and the impact theory is used to describe electron broadening. To assess the influence of this assumption, two additional grids of line profiles have been computed within the present study using the standard theory, alongside those obtained from the simulations. One grid assumes that the impact approximation applies over the entire profile, while the other employs an interpolation between the impact and one-electron regimes. By construction, the simulation method is expected to provide a more

natural and self-consistent description of the transition between these electronic broadening regimes.

Finally, a new wavelength grid has been constructed for each spectral line to ensure improved coverage of the profile compared to that used in B97. Particular attention is paid to regions where subtle features induced by ion dynamics or forbidden components are expected, especially at low densities where these effects are confined to narrow wavelength intervals. The same wavelength grid is adopted for a given transition at all densities and temperatures, thereby facilitating interpolation in the computation of synthetic spectra. Each grid consists of carefully selected wavelength points, designed to remain compatible with prior assumptions over a wide range of physical conditions, including typical line widths, density-dependent behavior, and the presence of forbidden components that may give rise to secondary maxima.

### 3.1. Statistical Distribution of the Electric Field Intensity

A standard validation of the simulation environment consists in comparing the statistical distribution of the electric microfield generated by the stochastic process with the corresponding theoretical expectations.

Figures 3 and 4 present a comparison between the ionic electric-field distribution derived by Hooper (1968) and that obtained from the ensemble of simulation volumes. The comparison is performed at three multiples of the time step, corresponding to the initial time, the midpoint, and the final time of the simulation, for two representative electron densities. At all sampled times, the simulated distributions are found to be essentially indistinguishable from Hooper’s analytical distributions. This result demonstrates, first, that the adoption of the Debye potential successfully reproduces the expected microfield statistics, in agreement with previous studies (Gigosos & Cardeñoso 1996; Gigosos et al. 2014; Cho et al. 2022). Second, it confirms that both the initialization procedure of the simulation volume and the continuous generation of new particles during the simulation lead to a stationary stochastic process. The electric-field distributions produced separately by ions and electrons are likewise found to be stationary.

Figure 5 shows the ionic electric-field distribution obtained by combining the full set of simulation volumes over all time indices. This representation provides access to the behavior of the distribution in the regime of highly improbable electric-field intensities, corresponding to the asymptotic tail that contributes to the far wings of spectral lines. As illustrated, the simulated distribution overlaps almost perfectly with the Hooper

distribution over the entire range, including the low-probability, high-field domain.

### 3.2. Autocorrelation vs. Power Spectrum Methods

The power spectrum method proves clearly advantageous in terms of signal-to-noise ratio compared to the method based on the autocorrelation function, as noted by Cho et al. (2022) for hydrogen lines. Figure 6 compares the profile of the  $\lambda 4471$  line at a temperature of 20,000 K and an electron density of  $10^{16} \text{ cm}^{-3}$  obtained using both methods. While the signal-to-noise ratio appears satisfactory on a linear scale, a significant noise-like structure becomes evident when examined on a logarithmic scale, as shown in Figure 7. Such a behavior may introduce artifacts into the modeled spectra of white dwarfs unless the noise is removed during a post-processing stage of the line-profile calculations, given that the strongest spectral lines dominate the opacity over wavelength intervals extending several tens of Angströms from their respective line cores.

An analytical model allows for a prediction of an oscillatory behavior of the line profile computed via the autocorrelation function. The model is not intended to quantify the numerical noise introduced by a finite number of simulation volumes or a discrete time step. Its more modest objective is to qualitatively assess the effect of a finite simulation time on the final line profile. Consider a spectral line whose profile is Lorentzian in shape, characterized by a width parameter  $a_\omega$  in the angular frequency domain, and centered at a frequency  $\omega_0$ . Its corresponding autocorrelation function is written as  $C(t) = e^{-(a_\omega + i\omega_0)t}$ . Restricting its Fourier transform to a finite time  $T$  introduces an oscillatory term in the profile:

$$I(\omega, T) = \frac{1}{\pi} \text{Re} \int_0^T dt e^{-(a_\omega + i\omega_0)t} e^{i\omega t} \\ = \frac{1}{\pi} \frac{a_\omega}{a_\omega^2 + (\omega - \omega_0)^2} (1 + \zeta(\omega)), \quad (29)$$

which is the product of the desired Lorentzian profile and a term describing the relative error induced by the finiteness of  $T$ :

$$\zeta(\omega) = e^{-a_\omega T} \left( -\cos((\omega - \omega_0)T) \right. \\ \left. + \frac{\omega - \omega_0}{a_\omega} \sin((\omega - \omega_0)T) \right). \quad (30)$$

In the wings of the line, where the deviation from the center greatly exceeds the characteristic width of the profile ( $|\omega - \omega_0| \gg a_\omega$ ), the second oscillatory

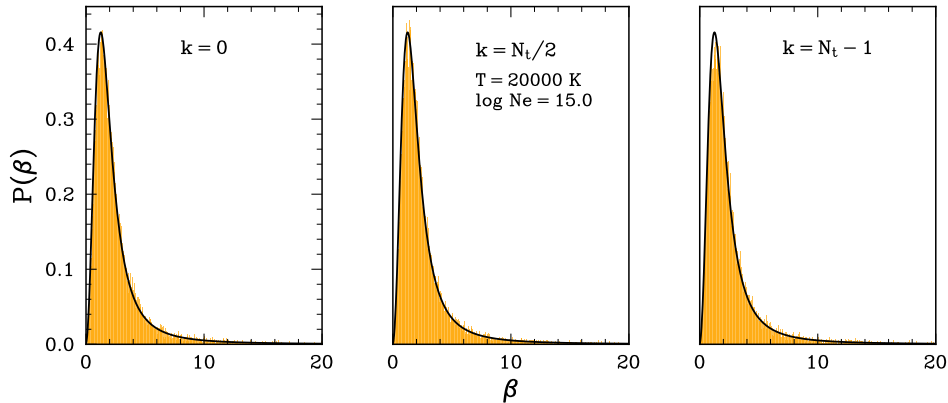


**Figure 3.** Microfield distribution for a temperature of 20,000 K and an electronic density of  $10^{15} \text{ cm}^{-3}$  at three time-step indices  $k = t_k/\Delta_t$  of 0,  $N_t/2$  and  $N_t - 1$ .  $\beta$  is the intensity of the electric field normalized by the Holtzmark field. The distribution from Hooper (1968) is shown in black, while the generated distribution is represented by the orange histogram.

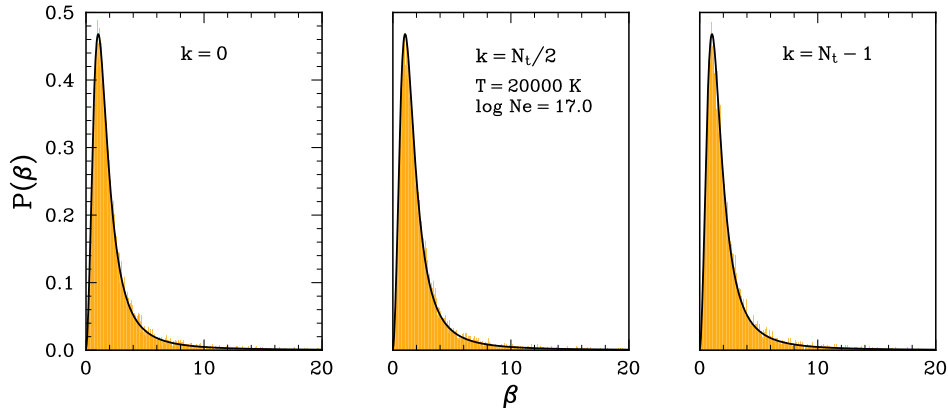


**Figure 4.** Same as Figure 3 but for an electronic density of  $10^{17} \text{ cm}^{-3}$ .

term becomes dominant, allowing the definition of a  $\omega$ -dependent amplitude of the oscillations

$$\zeta(\omega) = e^{-a_\omega T} \frac{|\omega - \omega_0|}{a_\omega}, \quad (31)$$

which rises above unity, thereby becoming the primary contributor to the numerical profile.

The Lorentzian shape is not valid in the wings of the  $\lambda 4471$  line, where the asymptotic behavior is governed by the linear Stark broadening due to ions, with  $I(\Delta\omega) \propto (\Delta\omega)^{-5/2}$ , in contrast with the Lorentzian form, which scales as  $\Delta\omega^{-2}$ . The linear behavior of the noise envelope in Equation (31), illustrated in Figure 8 for a generic spectral line, nevertheless reproduces the amplitude of the oscillations observed in Figure 7 for a specific choice of the model's input parameters. This does not rule out the possibility that a similar envelope is present with the power-spectrum method, although its amplitude appears to be negligible.

### 3.3. Normalization of the Profiles from the Standard Theory

The comparison between the profile sets obtained from the simulation and those derived from the semi-analytical method highlighted issues regarding the normalization of the latter. At low densities, the two approaches show excellent agreement except at the line cores, where ion dynamics—absent in the semi-analytical treatment—contribute. The primary discrepancies, however, arise at high densities, where several semi-analytical profiles display a systematic downward intensity shift (on a logarithmic scale) and a consistently smaller integrated area. This behavior underscores the need for a robust normalization strategy for semi-analytical profiles.

Two normalization procedures are commonly used in the context of the semi-analytical theory. The first is numerical normalization, which consists of integrating the unnormalized numerical profile over a frequency grid that accurately resolves the underlying continuous func-

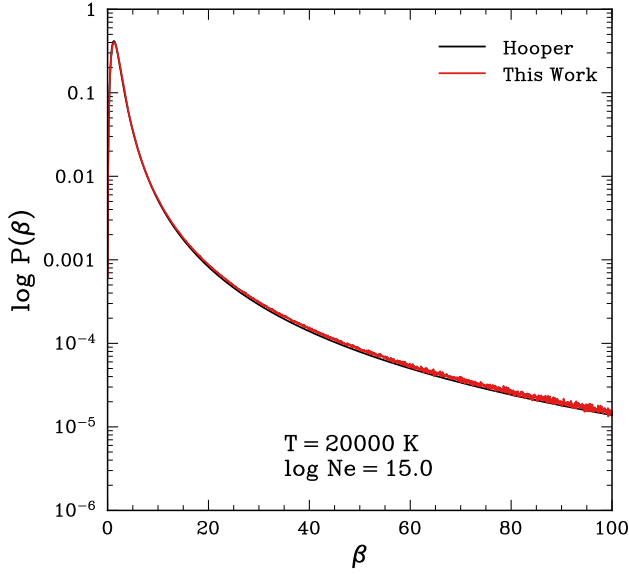


**Figure 5.** Microfield distribution for a temperature of 20,000 K and an electronic density of  $10^{15} \text{ cm}^{-3}$  over all time indices.

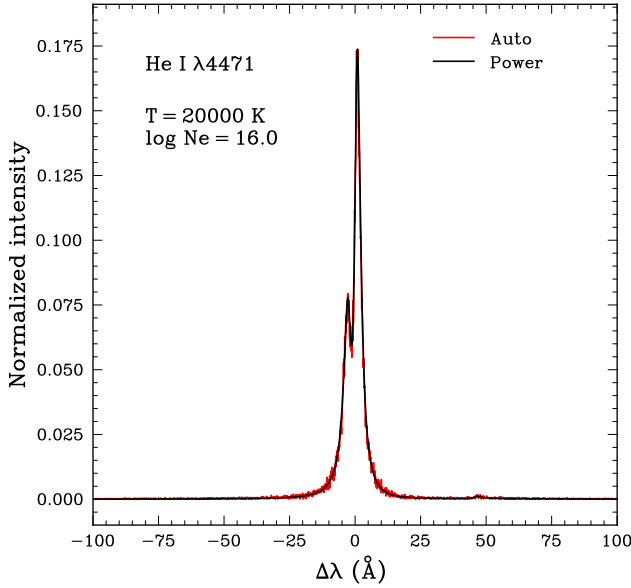


**Figure 6.** He I  $\lambda 4471$  line profile computed with the auto-correlation function and the power spectrum methods, for a temperature of 20,000 K and an electronic density of  $10^{16} \text{ cm}^{-3}$ .

tion. The frequency step must be significantly smaller than the characteristic Stark width near the core of the allowed components and of the strongest forbidden components, if present, at low density. The frequency range must also be sufficiently broad to capture the full profile at high densities. This procedure is applicable to both the semi-analytical theory and the simulation.

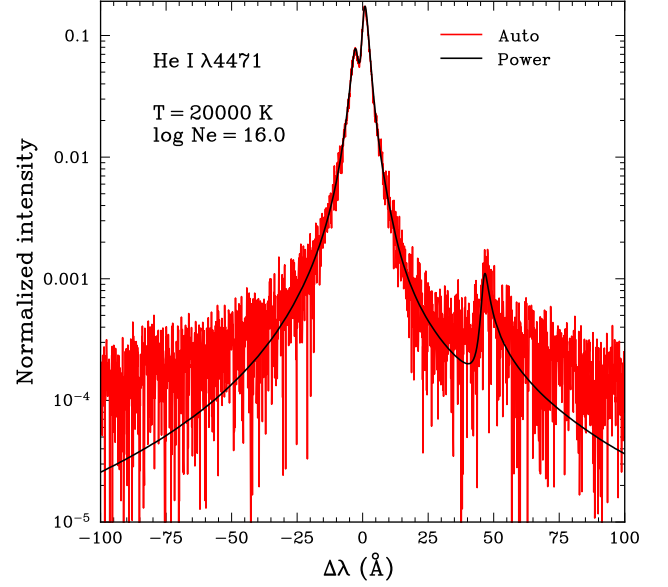


**Figure 7.** Same as Figure 6 but on a logarithmic scale.

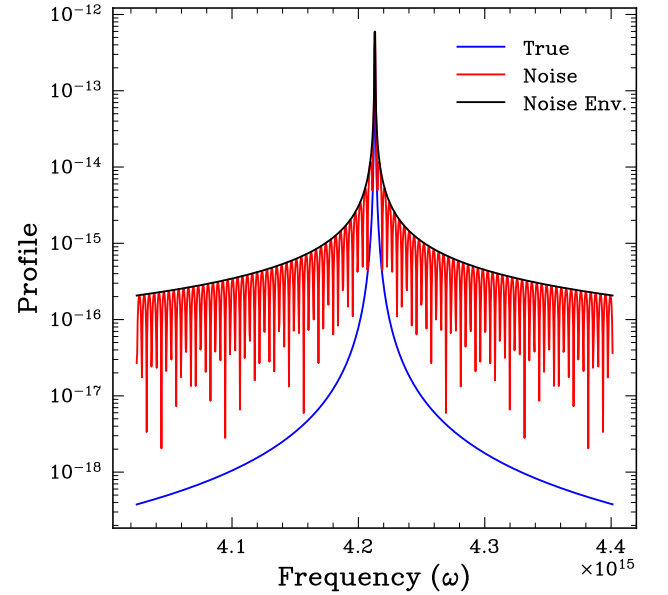


**Figure 8.** Profile of a generic line with a Lorentzian shape computed from truncated Fourier transform of the autocorrelation function (see text).

The second approach is specific to the semi-analytical model with electronic-impact broadening applied over the entire profile, thus excluding the one-electron description in the wings. In this method, the numerical profile (Equation 6) is divided by the sum of squared dipole matrix elements  $\sum_{ab} |\langle a | \mathbf{d} | b \rangle|^2$  (Kolb & Griem 1958). A key advantage of this approach is that the final frequency grid can be chosen freely without affecting the normalization.

However, the semi-analytical profiles computed here transition from electronic-impact broadening near the core to the one-electron theory in the wings, which invalidates the guarantee of proper normalization using the above procedure. This hybrid scheme was nonetheless adopted in the original work (B97), following the methodology of [Barnard et al. \(1974\)](#) and [Barnard et al. \(1975\)](#) for the  $\lambda\lambda 4471$  and  $4922$  lines, and of [Gieske & Griem \(1969\)](#), who introduced the Lewis cut-off ([Lewis 1961](#)) as an alternative but closely related transition scheme.

In the present study, a second version of the semi-analytical profile grid was therefore generated using numerical normalization. For each line, the sampling frequency grid was first validated by computing profiles broadened solely by electron impacts over the full frequency range. Across all tested lines, densities, and temperatures, the resulting profile areas were unity to within 1%. The final profile set—used as a benchmark against simulation-derived profiles—combined electronic-impact and one-electron contributions and was normalized numerically using the validated grid. It was found that certain lines, particularly those originating from upper levels with principal quantum numbers  $n = 5$  and  $6$  at the highest densities, required numerical normalization. Before normalization, the integrated areas of these lines were typically about  $0.9$  and  $0.8$  at  $N_e = 10^{17} \text{ cm}^{-3}$ , respectively. In contrast, the  $\lambda\lambda 4471$  and  $4922$  lines showed negligible differences between the two normalization methods.

### 3.4. Comparison of He I $\lambda\lambda 4471$ and $4922$

The validation of the calculated profiles in this work begins with a detailed comparison against profiles available in the literature. For neutral helium, numerical simulations providing detailed profiles are available only for He I  $\lambda 4471$  ([Gigosos & González 2009](#)) and  $\lambda 4922$  ([Lara et al. 2012](#)). These two sets of profile grids cover electron densities from  $10^{15}$  to  $10^{18} \text{ cm}^{-3}$ , approximately corresponding to the upper range of densities in our own set of profiles.

It is also instructive to compare our profiles with those of [Barnard et al. \(1974\)](#) and [Barnard et al. \(1975\)](#), who account for the contribution of ion dynamics using a procedure appropriate at low densities, while providing grids that extend to lower densities, from  $10^{13}$  to  $10^{16} \text{ cm}^{-3}$ . These grids therefore constitute a privileged reference for our profiles at lower densities, although ion dynamics is not included at their highest density point ( $10^{16} \text{ cm}^{-3}$ ). The B97 profiles cited in this section are those specifically regenerated for the present work, using the normalization procedure described in Section 3.3. In

all comparisons, Doppler broadening is applied consistently across profiles.

Figure 9 compares the  $\lambda 4471$  profiles from these authors with our results at electron densities of  $10^{14}$ ,  $10^{15}$ ,  $10^{16}$ , and  $10^{17} \text{ cm}^{-3}$ , and a temperature of  $20,000 \text{ K}$ . These four densities allow us to capture the full range of behaviors of interest and to highlight differences among the profiles reported by various authors. At the lowest density, our profile shows excellent agreement with [Barnard et al. \(1974\)](#), including the line core and the region between the allowed and nearest forbidden components, where ion dynamics contribute—an effect neglected in B97. The agreement remains excellent at  $10^{15} \text{ cm}^{-3}$ , this time including the results of [Gigosos & González \(2009\)](#). At  $10^{16} \text{ cm}^{-3}$ , our simulation profiles and those of [Gigosos & González \(2009\)](#) are nearly superimposed, whereas the profile of [Barnard et al. \(1974\)](#) aligns more closely with B97, both of which neglect ion dynamics. At the highest density, the profiles remain in good overall agreement, including in the wings, where the transition between the electronic-impact and one-electron regimes becomes significant in the standard theory as implemented by B97. Similar trends are observed for  $\lambda 4922$ , as shown in Figure 10.

The comparison of  $\lambda\lambda 4471$  and  $4922$  profiles, with and without ion dynamics, highlights two well-known phenomena at low densities when ion motion is accurately accounted for. First, the gap between the allowed component and its nearest isolated forbidden component is partially filled. Second, the forbidden component farthest from the line core (when sufficiently excited to be observable) exhibits a shallower slope on the side facing the allowed component. These effects are sufficiently pronounced to produce observable consequences in the spectra of low-gravity stars, where line formation occurs at densities on the order of  $10^{14} \text{ cm}^{-3}$  (see Sections 4.2 and 4.3).

To assess the electron contribution in the wings, Figure 11 compares He I  $\lambda 4471$  profiles at an electron density of  $10^{17} \text{ cm}^{-3}$  and  $20,000 \text{ K}$  using three approaches: the simulation, the semi-analytical theory with electronic-impact approximation only, and the semi-analytical theory including both impact and one-electron contributions. As shown, the impact theory predicts stronger wings and a shift of the He I  $\lambda 4517$  forbidden component, which is not consistent with the simulation results. This behavior is observed, and often more distinctly, in the majority of other spectral lines. Although not rigorously justified, interpolation between the two electron treatment approaches is therefore preferred, at least for the specific lines and thermodynamic conditions considered here.

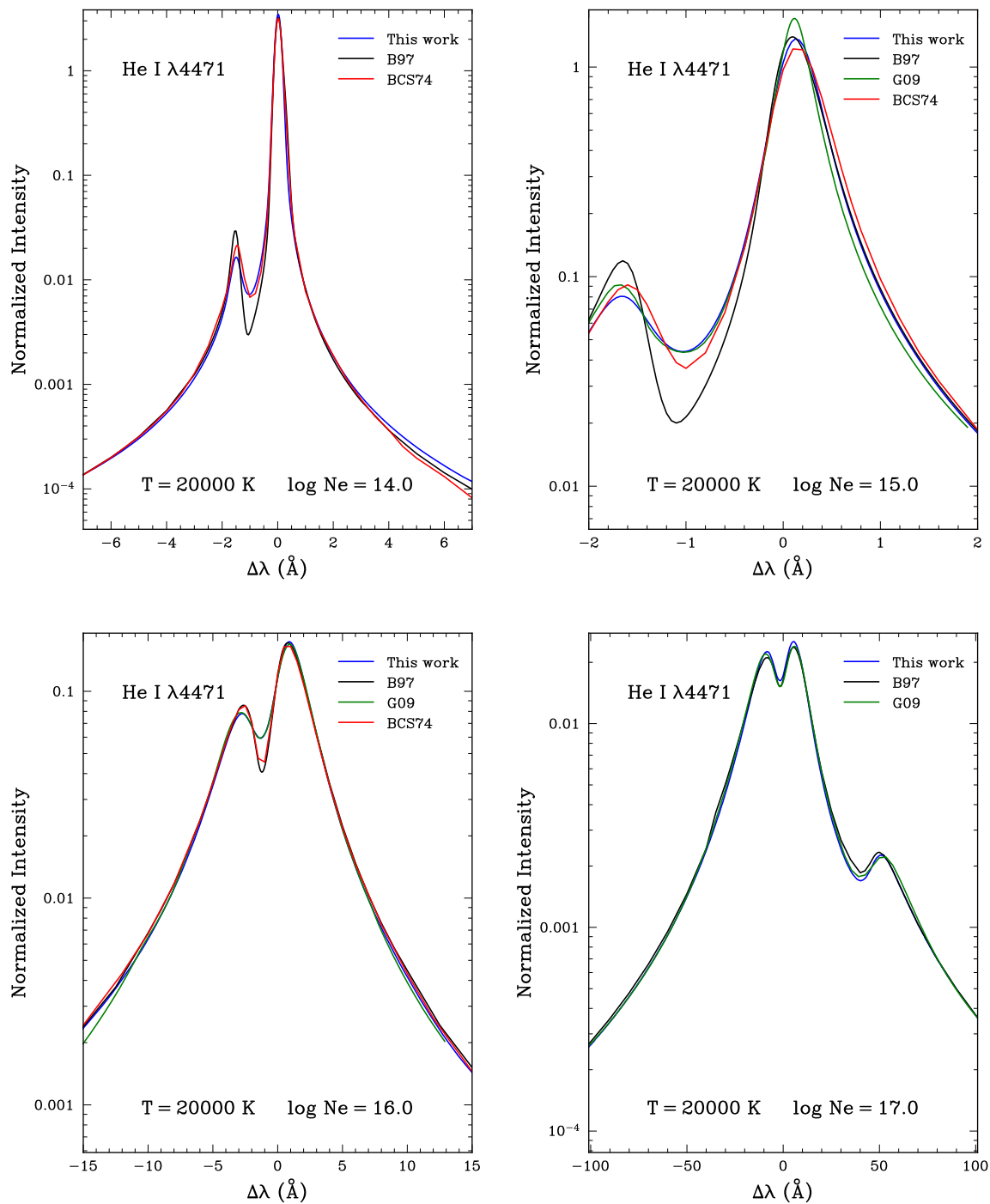


**Figure 9.** He I  $\lambda 4471$  line profile at densities ranging from  $10^{14}$  to  $10^{17}$   $\text{cm}^{-3}$  and a temperature of 20,000 K, from Barnard et al. (1974, BCS74), Gigosos & González (2009, G09), Beauchamp et al. (1997, B97), and this work.

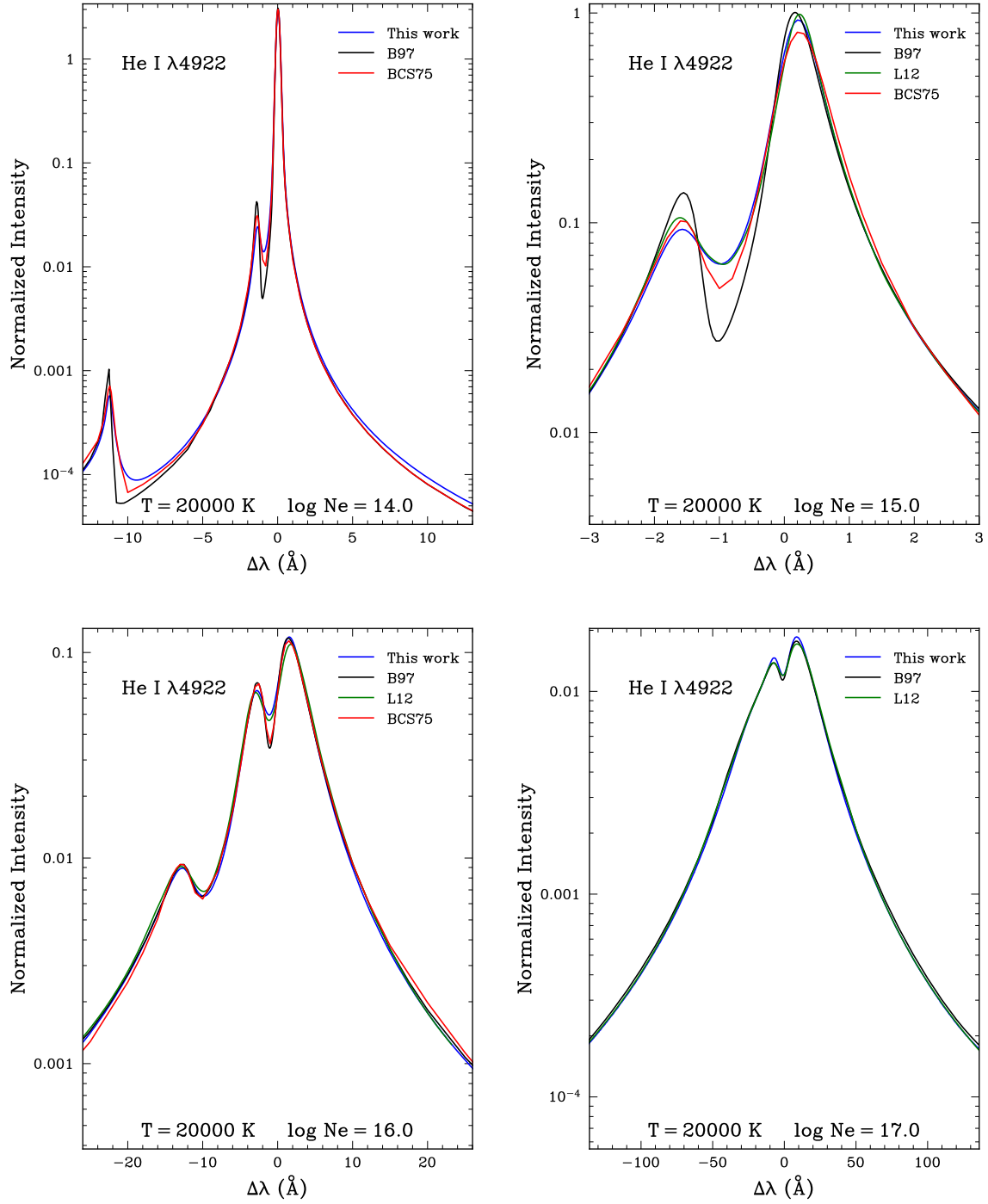


**Figure 10.** He I  $\lambda 4922$  line profile at densities ranging from  $10^{14}$  to  $10^{17} \text{ cm}^{-3}$  and a temperature of 20,000 K, from Barnard et al. (1975, BCS75), Lara et al. (2012, L12), Beauchamp et al. (1997, B97), and this work.

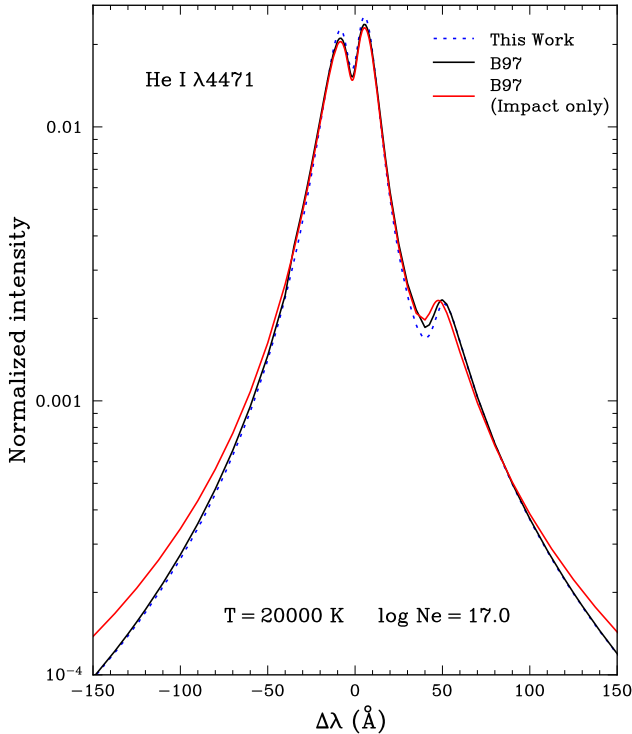


**Figure 11.** He I  $\lambda 4471$  line profile at a density of  $10^{17} \text{ cm}^{-3}$  and a temperature of 20,000 K, from [Beauchamp et al. \(1997, B97\)](#) with the semi-analytical theory including the impact approximation only as well as both impact and one-electron contributions, and this work.

### 3.5. Comparison Between Computer Simulations and Standard Theory for All Spectral Lines

An overview of the remaining He I lines, excluding  $\lambda\lambda 4471$  and  $4922$ , is presented to compare the predictions of the simulation model with those of the standard theory using proper normalization and incorporating the transition to the one-electron approximation in the line wings. All line profiles have been convolved with a Doppler broadening function.

Figures 12 to 14 display the profiles at an electron density of  $10^{16} \text{ cm}^{-3}$  and a temperature of 20,000 K. At this temperature and density, the two generations of profiles are nearly identical.

The comparison of high-density profiles allows identification of limitations in the transition procedure between the electronic-impact and one-electron regimes within the semi-analytical method as implemented in B97, and may provide guidance for future corrections. Figure 15 compares the profile of  $\lambda 4713$  at a density of  $10^{17.5} \text{ cm}^{-3}$  and 20,000 K. The B97 profile exhibits a discontinuity in the derivative at approximately  $80 \text{ \AA}$  from the line core on both sides. As discussed in B97, their interpolation scheme between electronic regimes uses non-

differentiable functions (absolute value and Max functions). In contrast, the profiles obtained from numerical simulations naturally transition between regimes and could serve as a reference for developing a more robust method in the future.

An alternative representation of the compared profiles is provided by a heat map, which illustrates the relative differences between the two sets of profiles across the full range of densities at constant temperature. This visualization highlights broader systematic effects that may be overlooked when examining individual profiles at specific densities.

Figures 16 and 17 employ a color scale to encode the relative difference: blue indicates that the line intensity at a given wavelength is greater in the profile obtained in this work compared to B97, whereas red indicates the opposite. The range of red intensities is configured to be narrower than that of the blue intensities.

As discussed previously, semi-analytical profiles often display near-discontinuities around distant forbidden components. Incorporating ion dynamics mitigates these irregularities by broadening the affected regions. All lines consequently exhibit narrow blue strips, either near the core or adjacent to forbidden components, frequently paired with a red band. This pattern reflects a redistribution effect required to approximately conserve the area of each component. Focusing on the forbidden components, substantial differences persist up to densities of  $10^{16.5} \text{ cm}^{-3}$ , at which point the effect of ion dynamics becomes negligible. A similar trend is observed for the core components of certain lines, notably  $\lambda 4471$  and  $\lambda 4922$ .

## 4. APPLICATIONS

In this section, we present several applications of our new Stark-broadening calculations for neutral helium lines. The first concerns white dwarf stars, for which the semi-analytical line profiles from B97 have been widely adopted. Because these are high-gravity objects, the improved treatment of ion dynamics is not expected to produce a significant change in the line profiles. However, ion dynamics is expected to play an important role in the next two low- $\log g$  objects: the ultraviolet-bright star Bernard 29 in the globular cluster M13 ([Dixon et al. 2019](#)), and the extreme helium-strong star HD 144941 ([Przybilla et al. 2021](#)).

### 4.1. White Dwarf Spectra

The semi-analytical He I Stark profiles from B97 have been employed in several comprehensive spectroscopic analyses of large samples of DB white dwarfs, notably in the Palomar-Green ([Bergeron et al. 2011](#)) and SDSS

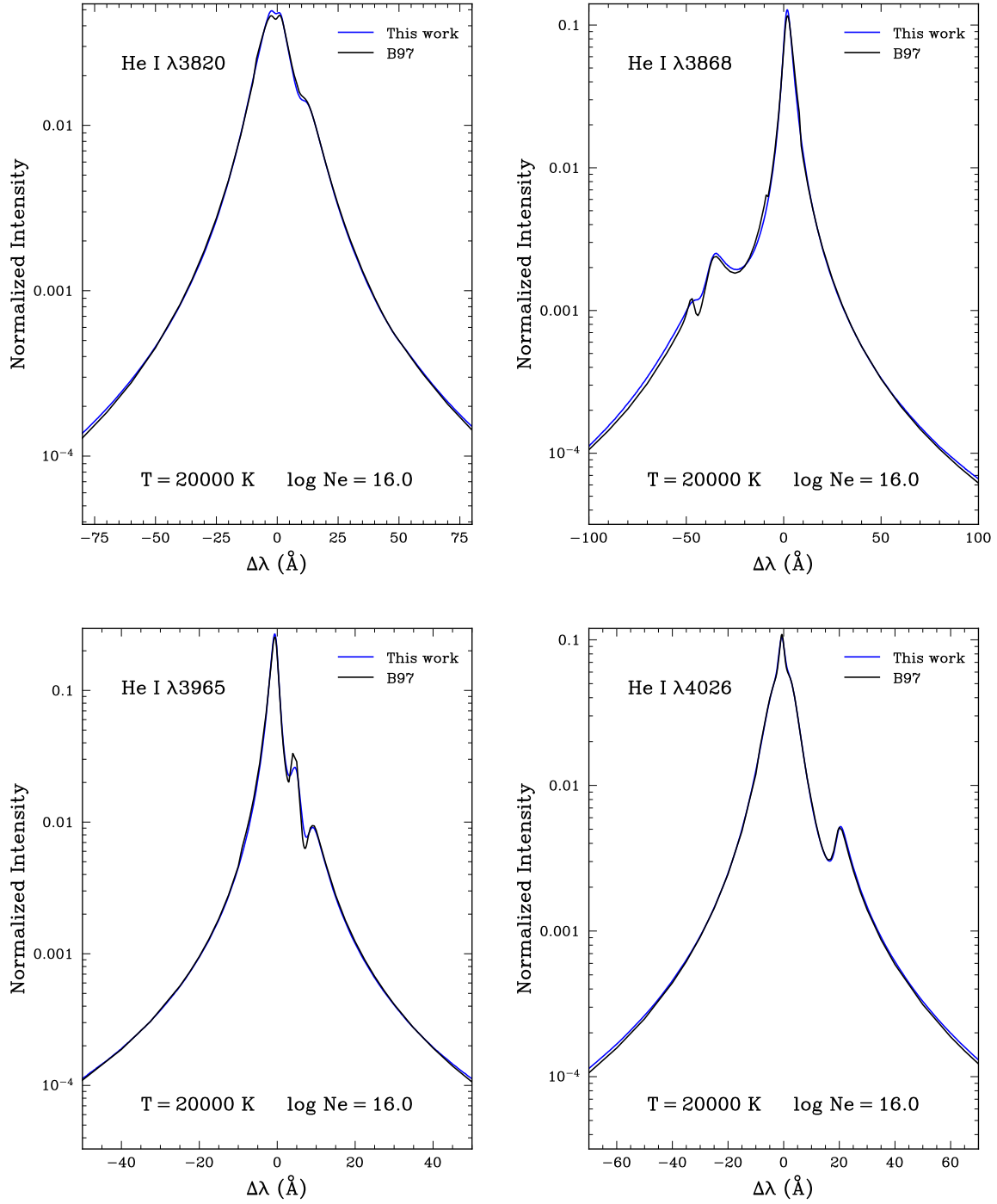


**Figure 12.** He I line profiles (indicated in each panel) at an electron density of  $10^{16}$   $\text{cm}^{-3}$  and a temperature of 20,000 K, from Beauchamp et al. (1997, B97) and this work.

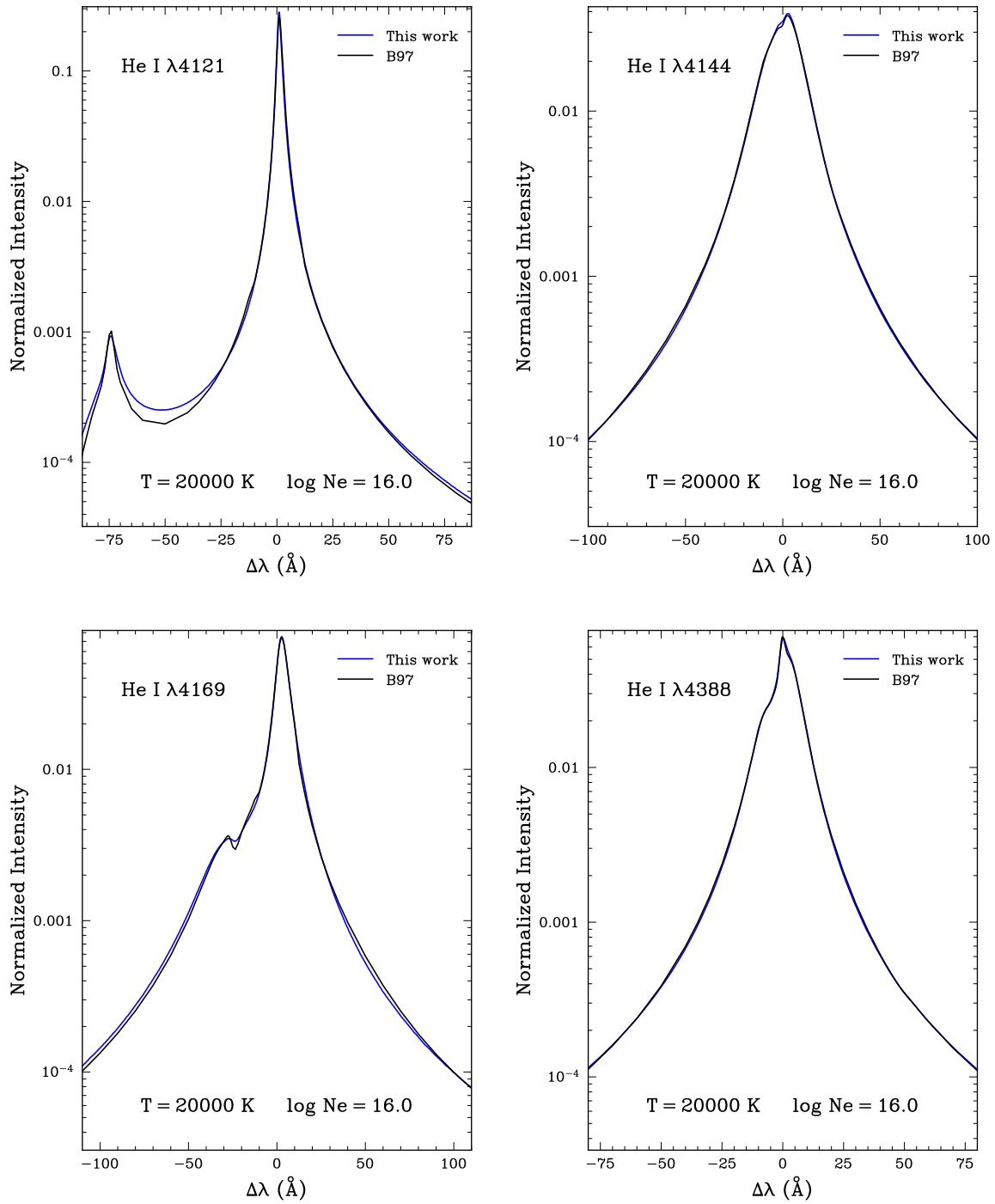


Figure 13. Same as Figure 12.

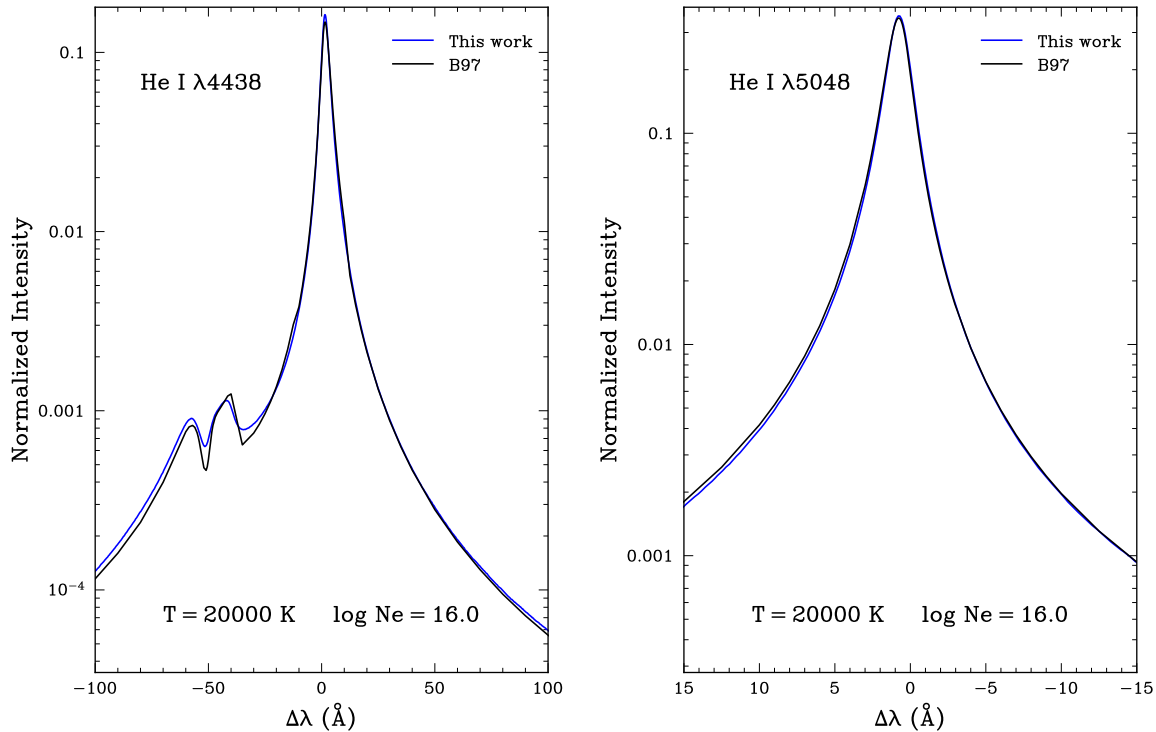


Figure 14. Same as Figure 12.

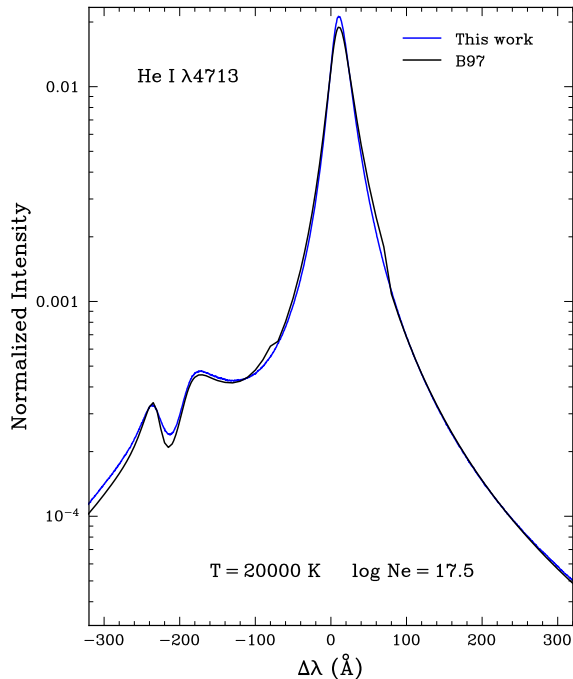
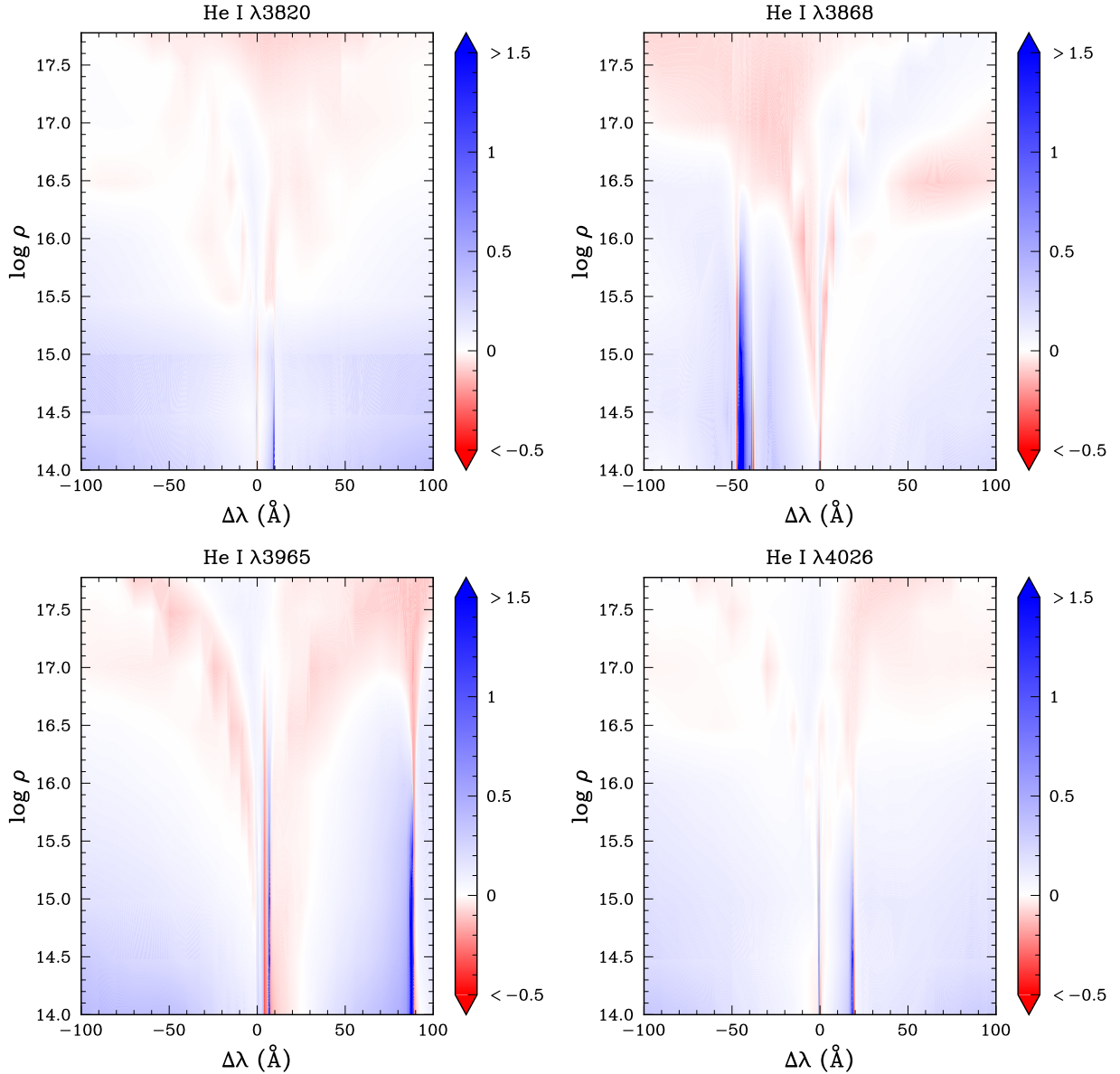


Figure 15. He I  $\lambda 4713$  line profile at an electron density of  $10^{17.5} \text{ cm}^{-3}$  and a temperature of 20,000 K, from [Beauchamp et al. \(1997, B97\)](#) and this work.

([Genest-Beaulieu & Bergeron 2019](#)) surveys. In these studies, the atmospheric parameters—effective temperature, surface gravity, and hydrogen-to-helium abun-

dance ratio—are derived using the spectroscopic technique, in which observed optical spectra are matched to model predictions through a  $\chi^2$  minimization procedure (see [Bergeron et al. 2011](#) for details). The model spectra are obtained by solving the radiative transfer equation using thermodynamic structures (temperature and pressure as functions of optical depth) provided by model atmosphere calculations. As a result, the synthetic spectra sample a broad range of physical conditions throughout the stellar atmosphere, in contrast to the illustrative examples presented above, which correspond to single values of temperature and electron density.

Figure 18 presents a comparison of synthetic spectra computed using the LTE model atmosphere code of [Bergeron et al. \(2011\)](#) for pure helium compositions at  $\log g = 8$  and effective temperatures spanning the range characteristic of helium-line (DB) white dwarfs in which Stark broadening dominates ( $15,000 \lesssim T_{\text{eff}} \lesssim 40,000 \text{ K}$ ). The spectra were calculated using both the B97 line profiles and our improved Stark profiles derived from computer simulations; results obtained at other values of  $\log g$  are qualitatively similar. It should be noted that the semi-analytical profiles adopted here are not identical to those originally published in B97, but incorporate several refinements motivated by comparisons with our simulation-based profiles (see Section 3.3). Since line dissolution is not included in our



**Figure 16.** Heat map (see text) for He I  $\lambda\lambda 3820, 3868, 3965$  and  $4026$  at electron densities ranging from  $10^{14}$  to  $6 \times 10^{17} \text{ cm}^{-3}$  and a temperature of 20,000 K, from [Beauchamp et al. \(1997, B97\)](#) and this work.

simulations, it has also been omitted from the B97 profiles to ensure a consistent comparison.

As expected, at the typical electron densities found in DB white dwarf photospheres ( $N_e \sim 10^{17} \text{ cm}^{-3}$ ), the semi-analytical B97 profiles and the simulated profiles are nearly indistinguishable. In this regime, the effects of ion dynamics are therefore negligible. This close agreement not only confirms the robustness of the B97 calculations, but also provides an important validation of our numerical simulations. In the context of white dwarf atmospheres, however, the inclusion of line dissolution remains a crucial ingredient. While it can be readily incorporated into the semi-analytical profiles

(see equations 4.1 and 5.5 of B97), it is not yet implemented within our current simulation framework.

For completeness, Figure 19 shows the best fits obtained for a representative DB white dwarf (SDSS J011657.85+073111.7) from the SDSS Data Release 17 (DR17), using model spectra computed with both the B97 and the simulation-based He I profiles. The resulting fits are qualitatively very similar, and the inferred atmospheric parameters differ only marginally, with the simulation-based profiles yielding an effective temperature higher by  $\sim 100$  K and a surface gravity larger by 0.03 dex. A comprehensive analysis of the full sample of DB white dwarfs identified in SDSS DR17,

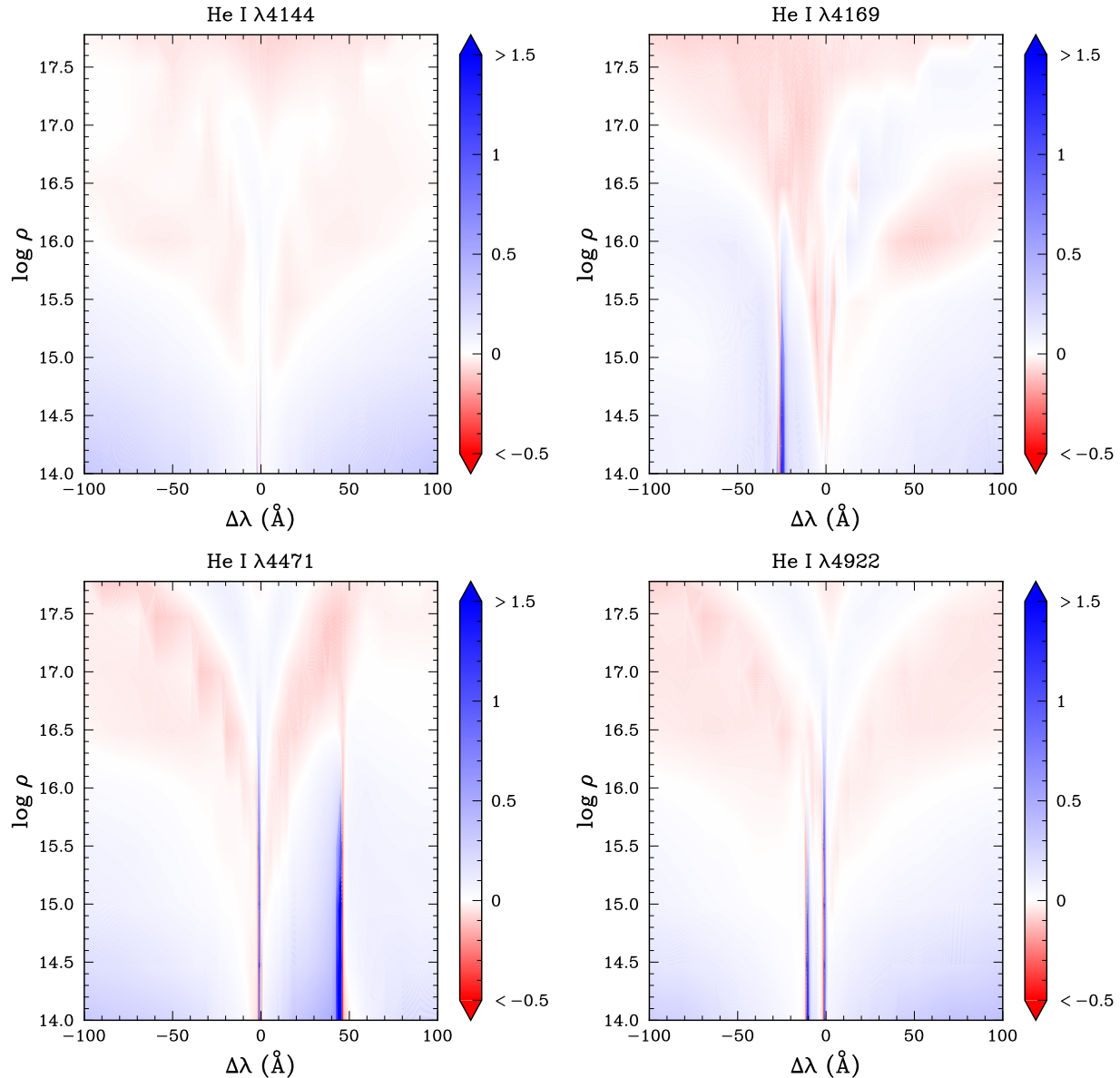


**Figure 17.** Same as Figure 16 but for He I  $\lambda\lambda$ 4144, 4169, 4471 and 4922.

based on both sets of line profiles, will be presented in a forthcoming paper.

#### 4.2. *Barnard 29*

Dixon et al. (2019) present a detailed analysis of several high-quality spectra of the UV-bright star Barnard 29, located in the globular cluster M13 (NGC 6205), including a very high-resolution spectrum obtained with the Keck High Resolution Echelle Spectrometer (HIRES). They derive atmospheric parameters of  $T_{\text{eff}} = 21,400 \pm 400$  K,  $\log g = 3.10 \pm 0.03$ , and  $\log N(\text{He})/N(\text{H}) = -0.89$ , by comparing photospheric abundances of various elements and by fitting the Balmer lines. In their analysis, NLTE model atmo-

spheres are computed using version 205 of the TLUSTY program (Hubeny & Lanz 1995), while synthetic spectra are generated with version 51 of the SYNSPEC program (Hubeny 1988). Their Figure 6 (see also their discussion in Section 4.1.2) presents the best fit to the He I lines observed in the optical HIRES spectrum of Barnard 29. They also discuss the difficulty in reproducing the forbidden components in the blue wings of He I  $\lambda$ 4388 and  $\lambda$ 4922. An improved fit to the He I  $\lambda$ 4922 feature (see their Fig. 7) is obtained by replacing the line profiles from Shamey (1969) in SYNSPEC with those from Barnard et al. (1975), which are computed for lower electron densities of  $10^{13} \text{ cm}^{-3}$ , characteristic of the line-forming region in Barnard 29. However, as

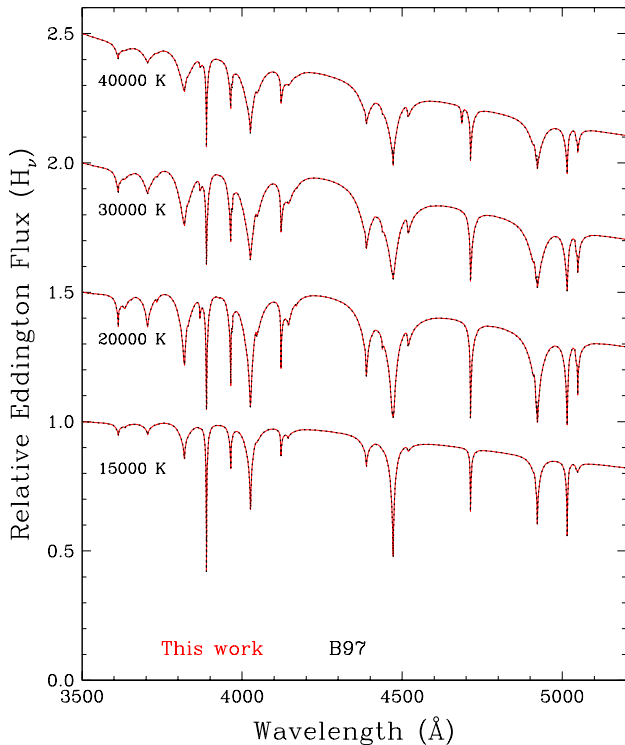


**Figure 18.** Comparison of pure helium synthetic spectra in the optical wavelengths calculated using He I Stark profiles from this work (solid red lines) and [Beauchamp et al. \(1997, B97; dotted black lines\)](#) at  $\log g = 8$  and various effective temperatures indicated in the figure. For the purpose of this comparison, line dissolution has not been included in any of these calculations.

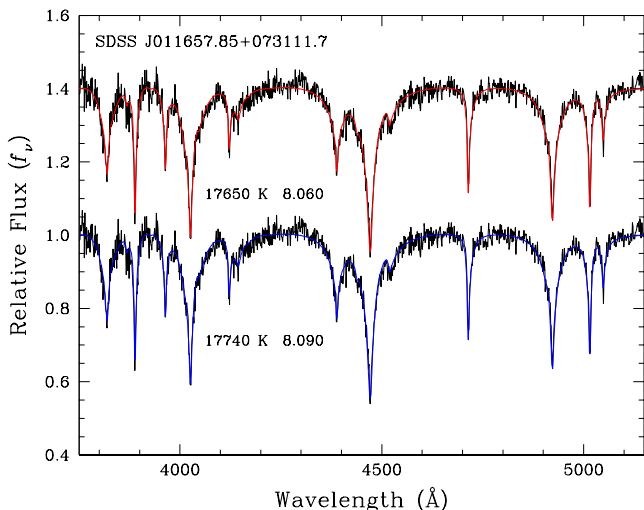


**Figure 19.** Best fits to a representative DB white dwarf in the Data Release 17 of SDSS using pure-helium model spectra calculated with the He I Stark profiles from B97 (red) and this work (blue); line dissolution is neglected in both cases. The  $T_{\text{eff}}$  and  $\log g$  values for each fit are given in the figure.

noted by [Tremblay et al. \(2020\)](#), the line profiles from these two sets of calculations also differ in their underlying physical assumptions. In particular, the profiles from [Barnard et al. \(1975\)](#), based on the work of [Barnard et al. \(1974\)](#), incorporate the one-electron approximation of [Baranger \(1962\)](#), which provides a more accurate transition between the impact approximation and the quasi-static contribution of the electrons, as well as corrections for ion dynamics.

In this work, we reanalyze the HIRES spectrum of Barnard 29 (kindly provided by P. Chayer), using the same versions of TLUSTY and SYNSPEC, into which we have incorporated our own sets of He I Stark profiles (see [Bédard et al. 2020](#) for details). We adopt the same atmospheric parameters as [Dixon et al. \(2019\)](#) given above. Figure 20 compares model spectra computed with SYNSPEC using the He I Stark profiles from B97 and those derived from our computer simulations for three neutral helium lines of interest: He I  $\lambda\lambda 4388$ , 4471, and 4922. For this low- $\log g$  star, our improved line profiles provide a significant improvement over the semi-analytical profiles for He I  $\lambda\lambda 4471$  and 4922, owing to the explicit inclusion of ion dynamics in our simulations. It is worth noting that [Dixon et al. \(2019\)](#) already obtained a satisfactory fit for He I  $\lambda 4471$  (see their Fig. 6); however, this result stems from their use of the line profiles from [Barnard et al. \(1974\)](#), which already include partial corrections for ion dynamics, as discussed above. By contrast, the effects of ion dynamics on He I  $\lambda 4388$  (bottom panel of Fig. 20) are less pronounced. We also note that the weak forbidden component of this line is reasonably well reproduced by both sets of calculations, in contrast to the results of [Dixon et al.](#), where this feature is not predicted (see the top panel of their Fig. 6).

Two distinct improvements are identified, consistent with the effects produced by ion dynamics, as discussed in Section 3.4. These effects have long been recognized for the  $2P^3 - 4D^3$   $\lambda 4471$  transition, where the gap between the allowed component and the  $2P^3 - 4F^3$   $\lambda 4470$  forbidden component is partially filled. A similar behavior is observed for the  $2P^1 - 4D^1$   $\lambda 4922$  transition, together with its associated forbidden components  $2P^1 - 4F^1$   $\lambda 4921$ . The He I  $\lambda 4388$  line exhibits more subtle differences, primarily resulting in a smoothing of the blend formed by the  $2^1P - 4^1F$  and  $2^1P - 4^1G$  forbidden components located approximately  $0.5 \text{ \AA}$  from the line core.

Since the dominant charged perturbers in this atmosphere are protons rather than singly ionized helium (He II), the contribution of ion dynamics is expected

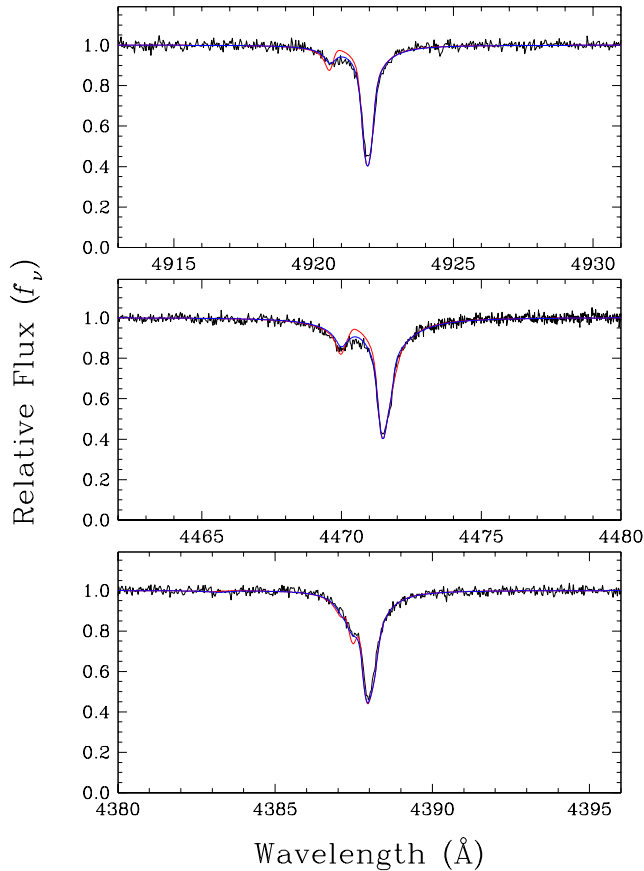


**Figure 20.** Comparison of the optical spectrum of the post-AGB star Barnard 29 (black) with synthetic spectra calculated using the He I Stark profiles from [Beauchamp et al. \(1997\)](#), (red) and this work (blue), both including Doppler broadening. The synthetic spectra are convolved with a Gaussian of FWHM = 0.1 Å to replicate the observed HIRES spectrum.

to be even more significant than in our current models. It would therefore be highly desirable to construct, in the future, a grid of Stark profiles similar to ours but explicitly including proton perturbers. The two upper panels of Figure 20 are consistent with a stronger contribution from ion dynamics, which would further fill the gap between the allowed and forbidden components and yield an even closer agreement with the observed spectrum.

#### 4.3. HD 144941

The second object investigated in this study is the extreme helium-strong star HD 144941, analyzed by [Przybilla et al. \(2021\)](#), who derived  $T_{\text{eff}} = 22,000$  K,  $\log g = 4.20$ , and a surface helium fraction of 0.950 by number, or  $N(\text{He})/N(\text{H}) \sim 20$ . Their quantitative spectroscopic analysis employed a hybrid NLTE approach in

which the thermodynamic structure of the atmosphere was computed under the assumption of LTE, while the emergent spectra were obtained from separate NLTE line-formation calculations. In the present work, we adopt the same full NLTE approach as for Barnard 29, and rely on our modified versions of TLUSTY and SYN-SPEC to compute model atmospheres and synthetic spectra using the atmospheric parameters determined by [Przybilla et al.](#)

We reanalyzed the optical spectrum of HD 144941 obtained with the Fibre-fed Optical Echelle Spectrograph (FEROS) mounted on the ESO–Max-Planck-Gesellschaft (MPG) 2.2 m telescope at La Silla (Chile), kindly provided by N. Przybilla. Figure 21 compares our best fits obtained with model spectra computed using the He I Stark profiles from B97 and those derived from our computer simulations, focusing on spectral regions around four neutral helium lines of particular interest: He I  $\lambda\lambda 4026$ , 4388, 4471, and 4922. In all cases, the profiles obtained from our simulations yield a noticeably better reproduction of the observed line shapes than the semi-analytical predictions, primarily as a result of the more realistic treatment of ion dynamics.

Because this star has a higher surface gravity than Barnard 29, additional forbidden components located farther from the line core become apparent. The additional discrepancies observed when comparing our newly computed profiles with those predicted by the semi-analytical approach are directly associated with these features. For the  $2P^3 - 4D^3$   $\lambda 4471$  transition, the  $2P^3 - 4P^3$   $\lambda 4517$  forbidden component exhibits a less abrupt left edge. A similar behavior is found for the  $2P^1 - 4D^1$   $\lambda 4922$  transition, where the second associated forbidden component,  $2P^1 - 4P^1$   $\lambda 4911$ , also displays a smoother profile. To our knowledge, this is the first time that such behavior has been successfully modeled for the  $\lambda 4026$  and  $\lambda 4388$  lines as well. In the case of  $\lambda 4026$ , the forbidden component  $2P^3 - 5P^3$   $\lambda 4045$  shows a noticeably smoother left slope compared to the prediction of the semi-analytical theory. Likewise, the forbidden component  $2P^1 - 4P^1$   $\lambda 4382$  is more accurately reproduced, including the shape of its right edge.

We note that the  $2P^1 - 7D^1$   $\lambda 4009$  line and the barely detectable  $2P^1 - 7S^1$   $\lambda 4024$  line remain unchanged, as these transitions were not included in the present simulation-based modeling.

## 5. CONCLUSION

In this work, we presented a new generation of Stark-broadened line profiles for 13 neutral helium transitions in the optical range, computed using modern computer-simulation techniques. By incorporating an

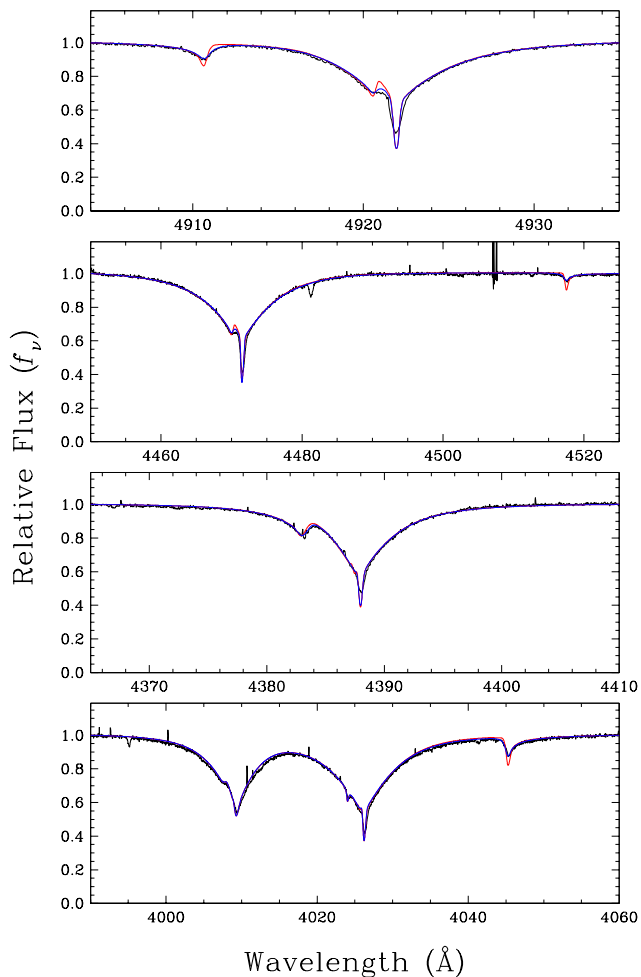


**Figure 21.** Comparison of the optical spectrum of the extreme helium-strong star HD 144941 (black) with synthetic spectra calculated using the He I Stark profiles from Beauchamp et al. (1997, red) and this work (blue), both including Doppler broadening. The synthetic spectra are convolved with a Gaussian of FWHM = 0.1 Å to replicate the observed FEROS spectrum.

improved particle reinjection scheme and an updated power-spectrum methodology, these calculations significantly extend the accuracy and physical realism of earlier simulation-based efforts. The resulting profiles exhibit more realistic wings at high density and an improved reproduction of forbidden components—features that collectively reduce several longstanding discrepancies when compared with the semi-analytical theory, as implemented by B97.

A detailed comparison with semi-analytical profiles based on the standard Stark broadening theory reveals that the simulations partially fill the gap between allowed and forbidden components at lower densities and modify the shape of several isolated forbidden compo-

nents. These effects were previously documented for He I  $\lambda 4471$  and  $\lambda 4922$ , but are modelled for the first time in this work for additional helium transitions. These differences directly impact spectral synthesis in astrophysical applications. Although the effects remain moderate in white dwarf atmospheres, they become more pronounced in lower-gravity objects, such as Barnard 29 and HD 144941, for which ion dynamics plays a larger role.

Despite these advances, the present simulations still lack the inclusion of line dissolution and strong-collision quantum corrections, and their accuracy may degrade at the highest densities investigated. Potential further improvements include the incorporation of multipole interactions (Gomez et al. 2016), the implementation of full Coulomb simulations (Stambulchik & Iglesias 2022), and the extension of the quantum-state basis to enable a more accurate computation of perturbed quantum states and their associated energies (Stambulchik & Maron 2013; Cho et al. 2022).

This study also highlights the challenges associated with generating narrow line profiles—primarily those occurring at low densities—using computer simulations. In this regime, hardware advancements are required to obtain accurate and statistically reliable line profiles. Alternatively, methods such as the frequency-fluctuation method (FFM, Gigos 2014; Ferri et al. 2014) might offer a viable solution for the lower-density parameter ranges. Nonetheless, the profiles presented here represent a substantial step toward more physically complete helium line grids. They also provide valuable guidance for further improvements of semi-analytical models, several of which were already implemented in this paper and are further discussed in a forthcoming paper.

Overall, the simulation grid developed here establishes a modern foundation for helium line-broadening calculations and offers a robust framework for future spectroscopic analyses of helium-rich stars. Its integration into atmospheric modeling codes will allow a more reliable evaluation of Stark broadening effects and help refine our understanding of the physical conditions in dense astrophysical plasmas.

#### ACKNOWLEDGEMENTS

This work was supported in part by the NSERC Canada and by the Fund FRQNT (Québec).

#### DATA AVAILABILITY

Both the semi-analytical (with and without line dissolution) and simulation He I line profiles are available

on Zenodo, which can be accessed via the following link  
[doi:10.5281/zenodo.18722143](https://doi.org/10.5281/zenodo.18722143).

## REFERENCES

- Alexiou, S., Glenzer, S., & Lee, R. W. 1999a, *PhRvE*, 60, 6238
- Alexiou, S., Sauvan, P., Poquérousse, A., Leboucher-Dalimier, E., & Lee, R. W. 1999b, *PhRvE*, 59, 3499
- Anderson, P. W. 1949, *Physical Review*, 76, 647
- Baranger, M. 1958a, *Physical Review*, 111, 481
- . 1958b, *Physical Review*, 111, 494
- . 1962, *Pure and Applied Physics*, 13, 493
- Barnard, A. J., & Cooper, J. 1970, *JQSRT*, 10, 695
- Barnard, A. J., Cooper, J., & Shamey, L. J. 1969, *A&A*, 1, 28
- Barnard, A. J., Cooper, J., & Smith, E. W. 1974, *JQSRT*, 14, 1025
- . 1975, *JQSRT*, 15, 429
- Beauchamp, A., Wesemael, F., & Bergeron, P. 1997, *ApJS*, 108, 559
- Beauchamp, A., Wesemael, F., Bergeron, P., & Liebert, J. 1995, *ApJL*, 441, L85
- Bédard, A., Bergeron, P., Brassard, P., & Fontaine, G. 2020, *ApJ*, 901, 93
- Bergeron, P., Dufour, P., Fontaine, G., et al. 2019, *ApJ*, 876, 67
- Bergeron, P., Ruiz, M. T., & Leggett, S. K. 1997, *ApJS*, 108, 339
- Bergeron, P., Saffer, R. A., & Liebert, J. 1992, *ApJ*, 394, 228
- Bergeron, P., Wesemael, F., Dufour, P., et al. 2011, *ApJ*, 737, 28
- Calisti, A., Stamm, R., & Talin, B. 1988, *PhRvA*, 38, 4883
- Cho, P. B., Gomez, T. A., Montgomery, M. H., et al. 2022, *ApJ*, 927, 70
- Cukanovaite, E., Tremblay, P.-E., Bergeron, P., et al. 2021, *MNRAS*, 501, 5274
- Dixon, W. V., Chayer, P., Reid, I. N., & Miller Bertolami, M. M. 2019, *AJ*, 157, 147
- Ferri, S., Calisti, A., Mossé, C., et al. 2014, *Atoms*, 2, 299
- Frerichs, M. R. 1989, *Zeitschrift fur Physik D Atoms Molecules Clusters*, 11, 315
- Genest-Beaulieu, C., & Bergeron, P. 2019, *ApJ*, 882, 106
- Gieske, H. A., & Griem, H. R. 1969, *ApJ*, 157, 963
- Gigosos, M. A. 2014, *Journal of Physics D Applied Physics*, 47, 343001
- Gigosos, M. A., & Cardeñoso, V. 1996, *Journal of Physics B Atomic Molecular Physics*, 29, 4795
- Gigosos, M. A., & Cardenoso, V. 1987, *Journal of Physics B Atomic Molecular Physics*, 20, 6005
- Gigosos, M. A., Djurović, S., Savić, I., et al. 2014, *A&A*, 561, A135
- Gigosos, M. A., Fraile, J., & Torres, F. 1985, *PhRvA*, 31, 3509
- Gigosos, M. A., & González, M. Á. 2009, *A&A*, 503, 293
- Gigosos, M. A., González, M. Á., & Cardeñoso, V. 2003, *Spectrochimica Acta*, 58, 1489
- Gomez, T. A. 2017, Ph.D. Thesis (University of Texas)
- Gomez, T. A., Montgomery, M. H., Nagayama, T., Kilcrease, D. P., & Winget, D. E. 2017, in *Astronomical Society of the Pacific Conference Series*, Vol. 509, 20th European White Dwarf Workshop, ed. P. E. Tremblay, B. Gaensicke, & T. Marsh, 143
- Gomez, T. A., Nagayama, T., Kilcrease, D. P., Montgomery, M. H., & Winget, D. E. 2016, *PhRvA*, 94, 022501
- Griem, H. R. 1974, *Spectral line broadening by plasmas* (New York: Academic)
- Halenka, J., & Olchawa, W. 1996, *JQSRT*, 56, 17
- Halenka, J., Olchawa, W., Grabowski, B., & Gajda, F. 2002, *JQSRT*, 74, 539
- Hegerfeldt, G. C., & Kesting, V. 1988, *PhRvA*, 37, 1488
- Hooper, C. F. 1968, *Physical Review*, 169, 193
- Hubeny, I. 1988, *Computer Physics Communications*, 52, 103
- Hubeny, I., & Lanz, T. 1995, *ApJ*, 439, 875
- Jeffery, C. S. 1998, *MNRAS*, 294, 391
- Jeffery, C. S., Scott, L. J. A., Philip Monai, A., Miszalski, B., & Woolf, V. M. 2024, *MNRAS*, 530, 1666
- Kolb, A. C., & Griem, H. 1958, *Physical Review*, 111, 514
- Lara, N., González, M. Á., & Gigosos, M. A. 2012, *A&A*, 542, A75
- Latour, M., Green, E. M., Dorsch, M., et al. 2025, arXiv e-prints, arXiv:2511.02539
- Lewis, M. 1961, *Physical Review*, 121, 501
- Liebert, J., Beaver, E. A., Robertson, J. W., & Strittmatter, P. A. 1976, *ApJL*, 204, L119
- Olchawa, W. 2002, *JQSRT*, 74, 417
- Olchawa, W., Olchawa, R., & Grabowski, B. 2004, *European Physical Journal D*, 28, 119
- Przybilla, N., Fossati, L., & Jeffery, C. S. 2021, *A&A*, 654, A119

- Rosato, J., Marandet, Y., & Stamm, R. 2020, JQSRT, 249, 107002
- Sahal-Brechot, S. 1969a, A&A, 1, 91
- . 1969b, A&A, 2, 322
- Seaton, M. J. 1990, Journal of Physics B Atomic Molecular Physics, 23, 3255
- Shamey, L. J. 1969, PhD thesis, University of Colorado at Boulder.
- Smith, E. W., Cooper, J., & Vidal, C. R. 1969, Physical Review, 185, 140
- Sorge, S., & Günter, S. 2000, European Physical Journal D, 12, 369
- Stambulchik, E., Fisher, D. V., Maron, Y., Griem, H. R., & Alexiou, S. 2007, High Energy Density Physics, 3, 272
- Stambulchik, E., & Iglesias, C. A. 2022, PhRvE, 105, 055210.  
<https://link.aps.org/doi/10.1103/PhysRevE.105.055210>
- Stambulchik, E., & Maron, Y. 2013, PhRvE, 87, 053108
- Stamm, R., & Smith, E. W. 1984, PhRvA, 30, 450
- Stamm, R., & Voslamber, D. 1979, JQSRT, 22, 599
- Tremblay, P., Beauchamp, A., & Bergeron, P. 2020, ApJ, 901, 104
- Tremblay, P. E., & Bergeron, P. 2009, ApJ, 696, 1755
- Wujec, T., Olchawa, W., Halenka, J., & Musielok, J. 2002, PhRvE, 66, 066403